Local structure and magnetism of La$_x$Eu$_{1-x}$PO$_4$ solid solutions

Laura Martel[1,*] Aydar Rakhmatullin,[2] José J. Baldoví,[3] Mauro Perfetti,[4] Karin Popa,[1] Michael Deschamps,[2] Thomas Gouder,[1] Eric Colineau,[1] Attila Kovács,[1] and Jean-Christophe Griveau[1]

[1]*European Commission, Joint Research Centre (JRC), Postfach 2340, D-76125 Karlsruhe, Germany*

[2]*Conditions Extrêmes et Matériaux: Haute Température et Irradiation, CEMHTI, UPR 3079 -CNRS Université Orléans 45071 Orléans, France*

[3]*Max Planck Institute for the Structure and Dynamics of Matter, Luruper Chaussee 149, 22761 Hamburg, Germany*

[4]*Department of Chemistry, University of Copenhagen, Universitetparken, 5, DK-2100 Copenhagen, Denmark*

By combining high spinning speed (60 kHz) and low-field (4.7 T) ^{31}P solid-state NMR with magnetic susceptibility measurements, we experimentally characterized a series of solid solutions belonging to the La$_x$Eu$_{1-x}$PO$_4$ ($0 \leqslant x \leqslant 1$) series. Analyses of the magnetic susceptibility data were carried out using the free ion model and crystal field theory calculations allowing to extract the electronic structure. The paramagnetic shifts of the P sites having one Eu^{3+} cation in their surrounding were predicted by combining the determined crystal field and energy level values with density functional theory (DFT) calculations. For the La$_{0.9}$Eu$_{0.1}$PO$_4$ sample, these theoretical shifts gave a very good overall trend allowing the unambiguous attribution of each P site. This study paves the way for the future analysis of both magnetic susceptibility and NMR data for a broad range of materials containing paramagnetic rare-earth cations.

I. INTRODUCTION

Owing to their technological and fundamental interest [1,2], lanthanide orthophosphates with the monazite crystalline structure (Ln = La to Gd) have been extensively studied over the past decades. The La$_x$Eu$_{1-x}$PO$_4$ solid solutions represent an important class of these materials, being luminescent [3–5] and being considered as potential matrices for encapsulation of nuclear materials due to their high resistance to radiation damage [6,7]. For this latter purpose, Eu^{3+} is, indeed, often used as a surrogate for Am^{3+} to monitor the structural modifications resulting from ion substitutions, as the two cations have similar outer electronic configuration (nf^6, $n = 4$ for Eu^{3+} and $n = 5$ for Am^{3+}) and ionic radii [8] (Eu^{3+} = $0.947-1.12$ Å and Am^{3+} = $0.975-1.09$ Å) [9–11]. Additionally, while a solid solution can generally be formed over the whole range of composition [12,13], in the focus are those with low rare-earth contents [1,4] as a high solubility in a LaPO$_4$ matrix does not occur for all lanthanide [14,15] or actinide [16–18] cations.

In order to have a better understanding of the local environment around the ^{31}P atoms in these solid solutions, magnetic angle spinning (MAS) NMR has been proven as an efficient analytical tool. Indeed, several authors published data on related crystalline rare-earth orthophosphates, like the LnPO$_4$ series (Ln^{3+} = La^{3+} to Eu^{3+} [19] and Ln^{3+} = La^{3+} to Yb^{3+} [20]) and some of their solid solutions (Ln^{3+} = Ce^{3+}, Nd^{3+}, and Gd^{3+}) [14,15,21]. It was shown that NMR allows to detect, in numerous types of materials, very low paramagnetic content in a unique manner [22]. However, a full attribution of the MAS- NMR signals is not straightforward because the paramagnetic cations cause additional contribution to the nuclear chemical shift [23]. Indeed, it is known that the experimental NMR shift (δ_{exp}) is the sum of an orbital component (δ_{dia}), a pseudocontact (PC) shift (δ_{PC}) and a Fermi contact (FC) shift (δ_{FC}) [24,25]. The determination of these paramagnetic shifts (δ_p) is currently based on a combination of empirical calculations using the Bleaney's theory for δ_{PC} [26,27] and the McConnell and Robertson approach and its recent improvements for δ_{FC} [28–34]. The theoretical prediction of paramagnetic shifts in the rare-earth series is intensively studied [24,35,36] especially for MRI contrast agents [37–44] and in metalloproteins [45–48]. However, these experiments are mostly performed using liquid-state NMR on organic molecules, usually containing conveniently one isolated paramagnetic cation. In inorganic materials, where several paramagnetic cations are present, the numerous unpaired electrons are difficult to handle in the calculations and therefore little has been achieved concerning the full prediction of the paramagnetic shifts [49,50].

Due to the difficulty encountered in predicting the paramagnetic shifts with the monazite crystallographic structure, it is often preferred to limit the discussions to the nature of the paramagnetic shifts through the full lanthanide series [14,15,50–52]. Thus, in their pioneering work, Palke and Stebbins attributed the nature of δ_p to arise from both FC and PC interactions in the La$_x$Ln$_{1-x}$PO$_4$ (Ln^{3+} = Nd and Ce) series [14,15]. This assumption was indirectly deduced from the analysis of the xenotime analogues (containing Ln^{3+} = Tb^{3+} to Lu^{3+}) which possess a more symmetric environment around the Ln^{3+} cation.

In the present study, we propose a combined experimental/theoretical approach to go further in the understanding of

*laura.martel@ec.europa.eu

the NMR data in the monazite series by considering this time the series $La_xEu_{1-x}PO_4$ (with $0 \leqslant x \leqslant 1$). To achieve this, we first probe the local environment using ^{31}P high-resolution MAS- NMR and low magnetic field. As numerous peaks are overlapping in most MAS- NMR spectra, we focus our data analysis on the two samples $La_{0.9}Eu_{0.1}PO_4$ and $La_{0.1}Eu_{0.9}PO_4$ while a more general discussion is presented about the remaining samples. In the next step, we predict the PC paramagnetic shifts of the P atoms surrounded by one paramagnetic center (vide infra) in these two compounds using calculated energy levels (EL) and crystal field parameters (CFP) obtained by fitting the experimental magnetic susceptibility curves. Finally, we determine indirectly the FC paramagnetic shifts for $La_{0.9}Eu_{0.1}PO_4$ from EPR parameters obtained by DFT calculations using its Gd^{3+} analogue.

II. METHODS

A. Synthesis

$LaPO_4$ and $EuPO_4$ as well as nine intermediate $La_xEu_{1-x}PO_4$ compositions of the solid solution were prepared by sol-gel reaction, using a procedure modified from Geisler *et al.* [13]. In short, stoichiometric amounts of La_2O_3 (Alfa Aesar, 99.99%) and Eu_2O_3 (Merck, 99.99%) were dissolved in HNO_3 (Merck, 63%). An excess of H_3PO_4 (Merck, 85%) (($Eu^{3+} + La^{3+}) : PO_4^{3-} = 1 : 1.2$) was added dropwise under continuous heating (343 K) and stirring; this initiated the precipitation of a white gel. After 1 h, a 25% NH_4OH solution (Merck) was added till achieving a pH = 5. The precipitates were separated from solution by centrifugation and subsequently washed several times with water. After drying in air, the powders were calcined for 5 h under air in alumina crucibles at 873, 1373, and 1873 K, with intermediate grinding steps.

B. NMR

The room temperature (334 K) ^{31}P MAS NMR spectra were recorded at 60 kHz on a Bruker AVANCE III HD 4.7 T spectrometer at a ^{31}P Larmor frequency of 81.02 MHz. One-pulse experiments were performed using a $90°$ pulse length of $1\,\mu s$. The longitudinal relaxation experiments were performed using a saturation-recovery pulse sequence. The variable temperature spectra were acquired at a spinning rate of 45 kHz. The temperature was calibrated with KBr using the linear law $T = -40\Delta\delta + T$ ($\Delta\delta$ being the shift variation and T the temperature) [53]. To be sure that KBr did not interact with the paramagnetic sample, a layer of Teflon film was added between the powders. All samples were referenced to H_3PO_4. The spectra were fitted using the DMFIT software [54].

C. Magnetic susceptibility

Measurements of the magnetic susceptibility (χ_{mol}) were performed by using a magnetic property measurement system (MPMS – Quantum Design) in the temperature range 2 to 300 K in applied magnetic fields between 0.5 and 7 T. The powders were pressed into pellets and put in a sample holder. The data obtained were then all corrected for the paramagnetic signal of the sample holder.

D. X-ray photoelectron spectroscopy (XPS)

The powder was pressed into indium foil (5×5 mm) and mounted on a stainless-steel sample holder. It was kept under vacuum at room temperature for 3 days. High-resolution XPS measurements were performed using a Phoibos 150 hemispherical analyzer. The Al K_α ($E = 1486.6$ eV) radiation was produced by an XRC-1000 microfocus source, equipped with a monochromator and operating at 120 W. The background pressure in the analysis chamber was 2×10^{-10} mbar. The spectrometer was calibrated with the $4f_{7/2}$ line of Au metal to give a value at 83.9 eV BE and the $2p_{3/2}$ line of Cu metal at 932.7 eV BE for XPS. Photoemission spectra were recorded at room temperature.

E. Calculations of the crystal field parameters and the energy levels

For the determination of the CFP data, we have used the SIMPRE computational package [55] introducing the experimental atomic crystallographic coordinates and applying the two fitting parameters [radial displacement vector (D_r) and the effective point charge (Z_i)] of the radial effective charge (REC) model [56]. The electronic structure of $La_{0.9}Eu_{0.1}PO_4$ has been calculated using the full basis of microstates in the latest version of the CONDON program [57].

F. DFT calculation of the EPR parameters

We firstly relaxed the $LaPO_4$ crystalline structure using geometry optimizations of the atomic positions (APO) with the QUANTUM ESPRESSO (QE) package [58–60] in order to remove the strain (from a computational point of view) from the experimental structure and to partly correct for the experimental uncertainties. QE relies on a pseudopotential plane-wave expansion formalism of density functional theory (DFT). A $4 \times 4 \times 4$ Monkhorst–Pack k-point grid and a kinetic energy cutoff of 100 Ry were used.

From the APO structure, we designed two cluster models of 54 (C1) and 77 (C2) atoms for the calculation of the EPR parameters shown in Fig. 4 and in Ref. [61]. The fixed cores of these clusters (12 and 47 atoms, respectively) correspond to the APO structure. The outer coordination sites are terminated by 21 and 15 OH groups, respectively. The geometrical parameters of the OH groups were relaxed by partial geometry optimizations using the GAUSSIAN 09 software [62]. The theoretical level of these calculations consisted of the B3LYP exchange-correlation functional in conjunction with the relativistic effective core potential of Hay and Wadt with the associated valence double-zeta basis set (LANL2DZ) for La and with the standard 6–31G** basis set for P, O, and H. The hyperfine tensors a_N (with and without spin-orbit effects) and the electron g tensor, or the g-shift tensor Δg (Δg predominant part arises due to spin-orbit effects [63,64]), were determined using the ADF code [65,66]. A previous work showed that this software was efficient for such calculations in the lanthanide series [63]. In these calculations, the scalar (SF) and spin-orbit (SO) relativistic effects were accounted for by utilizing the zeroth-order regular approximation (ZORA) [67]. The SAOP exchange-correlation potential [68,69] was applied, in conjunction with an uncontracted set of Slater-type

orbitals (STOs) of triple-zeta-plus-polarization quality (TZ2P-J) [70] containing extra tight (mainly $1s$) functions for use in EPR hyperfine calculations. As recommended for systems with heavy elements, the Gaussian finite nucleus model [71] was applied. For the calculation of the matrix products, the MATHEMATICA software was used [72].

III. RESULTS

A. Crystalline structure

The LnPO$_4$ (Ln = La, Eu) and their solid solutions [13] crystallize in the monazite space group $P21/n$. This crystallographic structure is composed of chains of alternating PO$_4$ tetrahedra and Ln-O$_9$ polyhedra along the c axis. With regard to crystallography, there is one P site, one Ln site and four different O sites. At the Ln site, a C_s (or C_{1h}) symmetry is formed as shown in Fig. 1 [73,74]. This symmetry is nonaxial and the symmetry operations are E and σ_H. Each Ln-O$_9$ polyhedron is surrounded in its first cation coordination shell by seven crystallographically distinct PO$_4$ (Fig. 1). The P-O-Ln distances (d_{POLn}) and angles are given in Table S1 [61]. While there is only one crystallographic P site in pure LnPO$_4$, we differentiate the seven P atoms as it will be necessary for the following NMR discussion on the solid solution.

By decreasing the cation size from La to Eu, the P-Ln distances decrease accordingly (cf. Table S1). The precise determination of the r_{P-Ln} distances in the solid solution

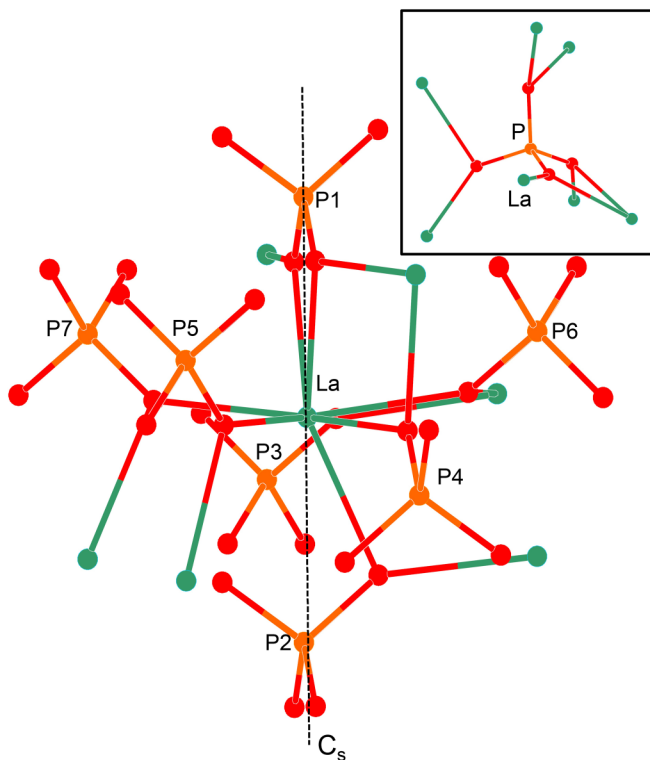samples was not possible. This is usually done via neutron diffraction experiments, which are particularly challenging for Eu-based materials because of their high cross sections. Nonetheless, it can be noticed that P1 and P2 are closer to the Ln cation with $r_{P-Ln} < 3.3$ Å, while P3 displays an intermediate distance of $r_{P-Ln} \sim 3.5$ Å and P4 to P7 have relatively similar distances with average distances of $r_{P-La} = 3.784$ Å and $r_{P-Eu} = 3.672$ Å for LaPO$_4$ and EuPO$_4$, respectively (see Table S1).

B. ^{31}P MAS NMR spectra

As a moderate magnetic field reduces the extent of the spinning sideband pattern and ultrafast MAS increases the spinning sideband separation (reduce their widths and increase coherence lifetimes) [75], the experiments were performed at 4.7 T at a spinning rate of 60 kHz. Moreover, as the frequency range can span around 50 kHz wide at this field, decreasing the spinning rate below 50 kHz or increasing the magnetic field would lead to the overlap between center peaks and spinning sidebands. The ^{31}P MAS NMR spectra of LaPO$_4$, EuPO$_4$ and their solid solutions are shown in Fig. S1 [61]. All experimental NMR parameters such as δ_{exp}, the paramagnetic shift δ_p (exp), the full width at half maximum, the relative intensities, and longitudinal relaxation times (T_1) are reported in Table I and Table S2 in Ref. [61]. All T_1 parameters were fitted using a single exponential time constant.

While the LaPO$_4$ and EuPO$_4$ spectra present a single peak at -4.5 ppm and 385.4 ppm, respectively (in agreement with the known unique crystallographic P site), the solid solutions spectra feature numerous peaks with pronounced overlapped and broadened features (Fig. S1). Thus we only fitted the spectra of La$_{0.9}$Eu$_{0.1}$PO$_4$ and La$_{0.1}$Eu$_{0.9}$PO$_4$ as shown in Fig. 2. For these two samples, only the quantitative spectrum of La$_{0.1}$Eu$_{0.9}$PO$_4$ presented remaining spinning sidebands, which have been included in the fit as shown in Fig. S2 [61]. The spectrum of La$_{0.9}$Eu$_{0.1}$PO$_4$ could be fitted using fifteen peaks as depicted in Fig. 2(a), and the one of La$_{0.1}$Eu$_{0.9}$PO$_4$ could be described by five peaks [Fig. 2(b)]. While an unambiguous fit cannot be obtained for all the spectra, it could be noticed that signals with similar δ_{exp} are clearly visible through the whole solid-solution composition range (Tables I and S1). For example, peaks 1 to 7 in La$_{0.9}$Eu$_{0.1}$PO$_4$ and La$_{0.8}$Eu$_{0.2}$PO$_4$ or peaks 1 to 5 in La$_{0.1}$Eu$_{0.9}$PO$_4$ and La$_{0.2}$Eu$_{0.8}$PO$_4$. Previous studies on solid solutions containing rare-earth elements have shown that finding similar NMR shifts is an evidence for the presence of a similar environment around the nucleus detected by NMR [50–52]. It should also be noted that the line broadening is more important for the Eu-rich solid solutions (Table I), as expected for solid solutions with higher paramagnetic cation content (structural local disorder and/or anisotropic bulk magnetic susceptibility effects) [14,15,21,49].

C. Magnetic susceptibility curves

Based on the NMR results, we decided to focus the magnetic susceptibility measurements on four specific samples to investigate a possible trend: LaPO$_4$, La$_{0.9}$Eu$_{0.1}$PO$_4$, La$_{0.5}$Eu$_{0.5}$PO$_4$, and La$_{0.1}$Eu$_{0.9}$PO$_4$ (Fig. S5 [61]). As the magnetic susceptibility of EuPO$_4$ has been previously measured

FIG. 1. Example of the C_s symmetry for the LaPO$_4$ crystalline structure represented by a 4.5-Å sphere with La as a central atom. The following color code is used: La atoms are in green, P atoms in orange, and O atoms in red. Here, the seven P sites have been differentiated to illustrate the discussion through the paper. In the insert is presented the local environment around the P atom.

TABLE I. Summary of the NMR parameters extracted from the experimental spectra: the measured experimental shift (δ_{exp}), experimental paramagnetic shift [δ_p (exp)], the full width at half maximum (FWHM), relative intensity (RI), and longitudinal relaxation time (T_1).

Sample composition	Peak	δ_{exp} (ppm) (± 0.2 ppm)	δ_p (exp) (ppm) (± 0.2 ppm)	FWHM (ppm) ($\pm 5\%$)	RI (%) ($\pm 1\%$)	T_1(s) ($\pm 5\%$)
LaPO$_4$						
	1	−4.5		2.5		1714
La$_{0.9}$Eu$_{0.1}$PO$_4$						
	1	220.1	225.2	13.5	4.9	0.296
	2	121.4	126.5	15.9	5.9	0.523
	3	42.0	47.1	10.1	5.3	1.7
	4	16.5	21.6	11	6.1	2.3
	5	−5.1	–	9.6	49.7	25.2
	6	−39.1	−34	10.6	9.9	3.3
	7	−62.6	−57.5	12	5.6	2.9
	8	335.7	–	17.5	0.9	
	9	273.3	–	12.8	0.6	
	10	193.5	–	9.2	0.9	
	11	164.1	–	11.9	1	
	12	85.25	–	21.6	1.8	
	13	2.96	–	7.8	3.7	
	14	−27.9	–	7.8	2.8	
	15	−96.9	–	15.4	0.9	
La$_{0.1}$Eu$_{0.9}$PO$_4$						
	1	386.4	391.5	51.5	75.9	0.215
	2	335	340.1	60.3	7.3	0.258
	3	229.5	234.6	40.2	7.3	0.396
	4	136.7	141.8	61.1	8.4	0.429
	5	−33.6	−28.5	38.9	1.1	–
EuPO$_4$						
	1	385.4		45.4		0.21

[76,77], the magnetic susceptibility curve acquired by Golbs *et al.* [77] was extracted and analyzed alongside the data we recorded for the other samples (Fig. S5). For LaPO$_4$, the experimental value of $\chi = -0.2 \times 10^{-3}$ emu mol^{-1} obtained is, as expected, characteristic of its diamagnetic behavior. A small diamagnetic upturn is also present (Fig. S5). The magnetic susceptibility curve of EuPO$_4$ is characteristic of a pure Van Vleck (VV) behavior with low-temperature independent variation up to ∼100 K (due to the diamagnetic $J = 0$ ground state of Eu^{3+}) [78], then it becomes temperature dependent. At higher temperatures, a Curie-Weiss like behavior is visible as observed in other Eu^{3+}-based material [78–80].

For a coherent approach, the magnetic susceptibilities of the solid solutions have also been normalized considering the Eu^{3+} content ($\chi_{mol.Eu3+}$) in Fig. 3. Above 50 K, all the solid solution curves present a typical VV paramagnetism even for the low Eu-content. Below 50 K, an upturn is clearly detected on all the recorded magnetic susceptibility curves. This upturn is more visible for the La$_{0.9}$Eu$_{0.1}$PO$_4$ composition [Fig. 3(b)]. It should be noted that for this low Eu^{3+}-doped sample, there is also the presence of a small amount of a ferromagnetic impurity characterized by a hysteresis loop at low field (Fig. S6 [61]). This ferromagnetic behaviour is suppressed at a magnetic field of 4.7 T, at which field the NMR experiments were conducted.

The effective moment at 300 K [$\mu_{eff} = \sqrt{8\chi_{300 K} T}$ in the centimetre-gram-second (CGS) system] has been determined

for all compositions considering the magnetic susceptibility value at this temperature. This was done considering χ_{mol} (μ_{eff}) and $\chi_{mol.Eu3+}$ ($\mu_{effEu3+}$). The values are reported in Table II. Through the series, there is a decrease of μ_{eff} with decreasing Eu-content as expected from the diamagnetic character of LaPO$_4$. The $\mu_{effEu3+}$ values are consistent with the value of 3.51 μ_B determined for a free Eu^{3+} ion [81,82], while they are slightly decreasing with decreasing Eu^{3+} content.

IV. DISCUSSION

A. Analysis of the ^{31}P MAS NMR data

1. The quantitative spectra

The spectra of the solid solutions with paramagnetic cations allow us to characterize the local structure around the NMR active spin-bearing nucleus in a unique manner [51]. Thus, in the ideal case of a randomly distributed network (RDN), depending on the composition of the solid solution, the NMR peaks can be assigned to P(La)$_m$(Eu)$_{7-m}$ ($0 \leqslant m \leqslant 7$) units (i.e., a P atom surrounded by "m" La atoms and "7-m" Eu atoms). Their relative intensities can be predicted thanks to the formula:

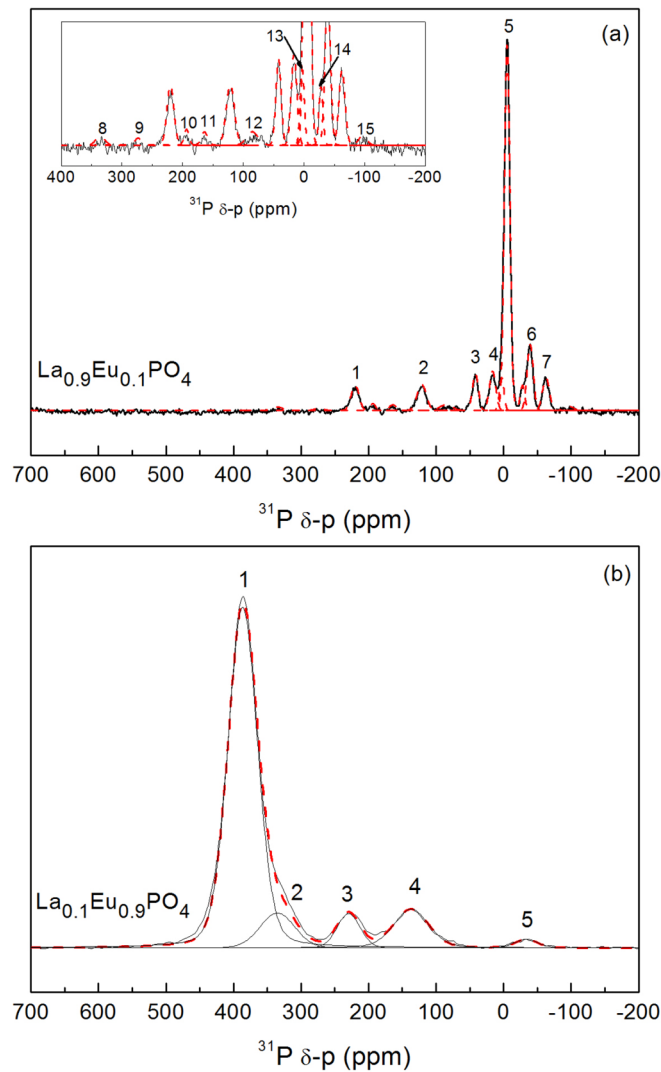$$I_k = (p^k(1-p)^{n-k})\left(\frac{n!}{k!(n-k)!}\right), \qquad (1)$$

FIG. 2. ^{31}P MAS NMR spectra of (a) La$_{0.9}$Eu$_{0.1}$PO$_4$ and (b) La$_{0.1}$Eu$_{0.9}$PO$_4$ and their corresponding fits acquired at 4.7 T at a MAS rate of 60 kHz. The insert shows an enlargement of the low intensity signals of La$_{0.9}$Eu$_{0.1}$PO$_4$.

where p is the probability of Ln^{3+} replacing an Eu-O$_9$ site, which is equal to the concentration of Eu^{3+}, $k = 7 - m$ is the number of Eu^{3+} interacting with the ^{31}P nucleus for the specific peak, n is the total number of sites into which Eu^{3+} can enter and cause a specific paramagnetically shifted peak (equal to 7 here for the seven distinct first-shell ^{31}P−Eu^{3+} configurations). With this approach, we obtained the values displayed in Table S3 [61]. Thus, for example, the spectrum of La$_{0.9}$Eu$_{0.1}$PO$_4$ should have four signals corresponding to the P(La)$_7$(Eu)$_0$, P(La)$_6$(Eu)$_1$, P(La)$_5$(Eu)$_2$, and P(La)$_4$(Eu)$_3$ units with the relative intensities of 48%, 37%, 13%, and 2%, respectively. Similarly, for La$_{0.1}$Eu$_{0.9}$PO$_4$, four signals with the same relative intensities are also expected except that they should correspond to the P(La)$_0$(Eu)$_7$, P(La)$_1$(Eu)$_6$, P(La)$_2$(Eu)$_5$, and P(La)$_3$(Eu)$_4$ units respectively. By comparing the experimental data with the theoretical number of peaks and relative intensities, one can but notice the differences. Indeed, the experimental spectrum of La$_{0.9}$Eu$_{0.1}$PO$_4$ presents
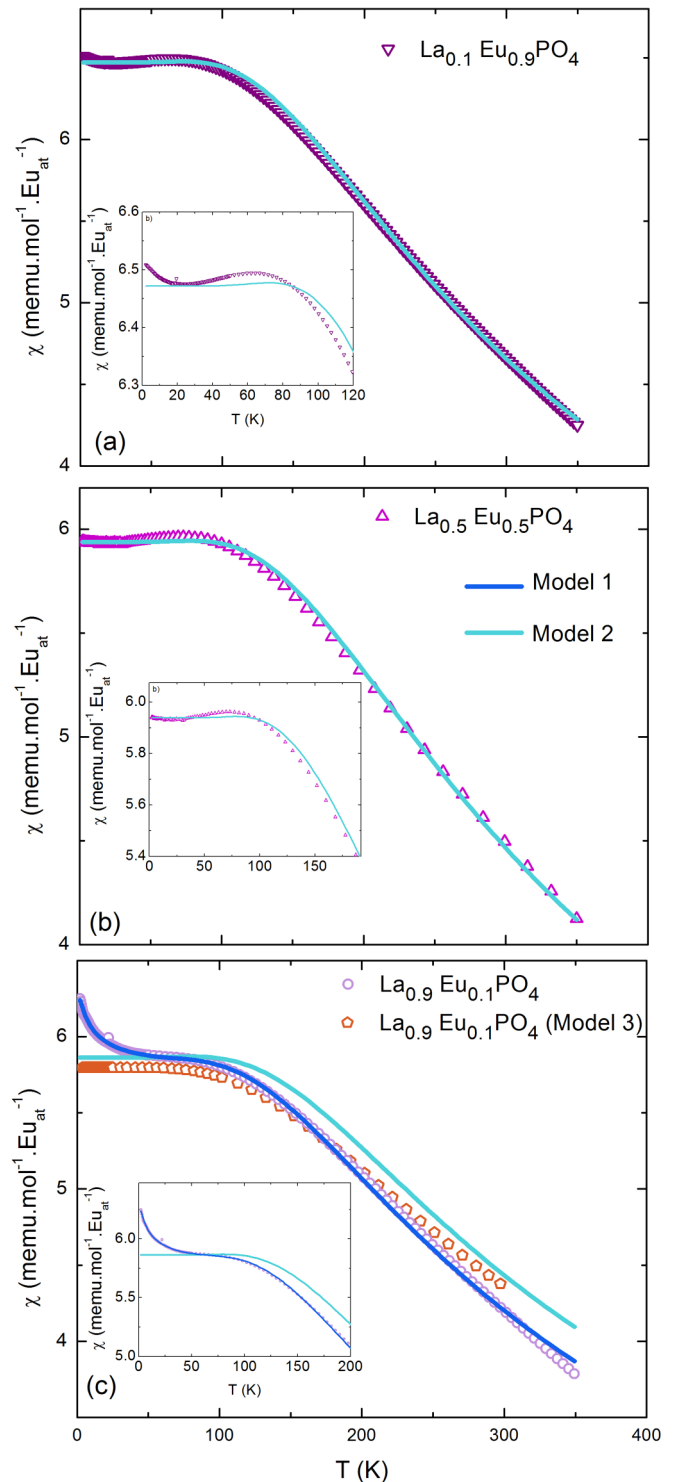

FIG. 3. Field cooled magnetic susceptibility curves of (a) La$_{0.1}$Eu$_{0.9}$PO$_4$, (b) La$_{0.5}$Eu$_{0.5}$PO$_4$, and (c) La$_{0.9}$Eu$_{0.1}$PO$_4$. To fit the $\chi_{\mathrm{mol.Eu3+}}$, we considered Model 1, Model 2, and approaches as discussed in the text. La$_{0.1}$Eu$_{0.9}$PO$_4$ calculated magnetic susceptibility based on Model 3 is included in (c).

15 peaks and the one of La$_{0.1}$Eu$_{0.9}$PO$_4$ five peaks with relative intensities different from the RDN values. A straightforward explanation to these differences can be deduced from the similar spectra previously recorded for the La$_x$Ce$_{1-x}$PO$_4$ monazite

TABLE II. Effective moments at 300 K for the solid solutions (μ_{eff}) and for the specific Eu^{3+} magnetic cation [μ_{eff} (mol Eu^{3+})$^{-1}$]. The $\lambda = E_1$ constant considering a free ion determined by fitting with Models 1 and 2 (see text).

			Model 1	Model 2			
Name	μ_{eff} (μ_B)	$\mu_{\text{effEu3+}}$ (μ_B)	λ (cm^{-1})	λ (cm^{-1})	C	θ_p	f_i
EuPO$_4$	3.39	3.39	278	260	0.015	-10	0.07
La$_{0.10}$Eu$_{0.90}$PO$_4$	3.17	3.34	322	–	–	–	–
La$_{0.50}$Eu$_{0.50}$PO$_4$	2.32	3.28	352	–	–	–	–
La$_{0.90}$Eu$_{0.10}$PO$_4$	1.01	3.18	356	327	0.058	-10	0.09

series (with $x = 0.97, 0.9, 0.84, 0.68$) [15]. Indeed, instead of having peaks with the relative intensities calculated with Eq. (1), the authors observed ($\frac{n!}{k!(n-k)!}$) peaks having each the relative intensity ($p^k(1-p)^{n-k}$). Consequently, depending upon the position of each Eu atom compared to the P atom a different NMR signal will be obtained. Now, taking again the La$_{0.9}$Eu$_{0.1}$PO$_4$ sample as an example and by considering the P(La)$_7$(Eu)$_0$ units (k = 0), the theoretical spectrum will be made of one signal with a relative intensity of about 48%. This theoretical value is in good agreement with the relative intensity of 49.7% determined experimentally for peak 5. The main difference with the values obtained from Eq. (1) will be indeed observed for $k \neq 0$ as it corresponds to the insertion of paramagnetic cations in the diamagnetic matrix. Thus, by considering now the P(La)$_7$(Eu)$_1$ units (k = 1), seven signals are expected with relative intensities of about 5.3% each. And it is exactly the relative intensities obtained for the experimental peaks 1–4, 6, and 7 (peak 6 being the overlapping of two components). Due to spatial inequivalency, 21 peaks for the P(La)$_5$(Eu)$_2$ units should appear on the spectrum, with relative intensities of 0.6%. Experimentally, some of these signals can be detected, but due to the low intensities, it will be difficult to analyze them further. Finally, the P(La)$_4$(Eu)$_3$ units will most probably not be detected as the calculated (RDN) relative intensity of 2% is divided over 35 peaks.

We also did a similar approach for the La$_{0.1}$Eu$_{0.9}$PO$_4$ spectrum. Thus, the observable signals should be: one peak for the P(La)$_0$(Eu)$_7$ units with a relative intensity of 48% and seven peaks for the P(La)$_1$(Eu)$_6$ units of about 5.3% each. It is clear that part of the signal intensity corresponding to peak 1 [Fig. 2(b)] belongs to the P(La)$_0$(Eu)$_7$ units as it is the most intense (77%). Unfortunately, it is here less straightforward to attribute the seven signals to the P(La)$_1$(Eu)$_6$ units mostly because the peaks are broad and overlapping. With these results in mind, one can easily understand the increased complexity observed in the spectra of the other solid solutions.

2. MAS- NMR spectra of other rare-earth monazites

For the low Eu^{3+} content, our spectrum can be compared to the one previously published for other La$_{0.9}$Ln$_{0.1}$PO$_4$ compounds (Ln = Ce [15] and Nd [14]). All the three spectra feature a similar unshifted peak with the highest relative intensity which can easily be attributed to the P(La)$_7$(Ln)$_0$ units. However, as expected, the peak positions of the seven P(La)$_6$(Ln)$_1$ units depend upon the nature of Ln^{3+} cation. Indeed, four peaks have positive frequencies for Eu^{3+} compared to the two ones for Ce^{3+} and to the three ones for Nd^{3+}. The other peaks

have negative shifts. A more detailed comparison between spectra from the same composition but with a different Ln^{3+} cation is not possible as the different peaks corresponding to these P(La)$_6$(Ln)$_1$ units were not previously assigned. To our knowledge, for such a high content of paramagnetic cation, only the La$_{0.25}$Nd$_{0.75}$PO$_4$ NMR spectrum has been published [20]. However, the authors did not achieve a sufficient spectral resolution due to the strong overlap between the main signal and the spinning sidebands.

3. Longitudinal relaxation times

A very long T_1 is observed for LaPO$_4$ (1714 s, see Table I) as expected for this diamagnetic compound [14]. Our value differs from the one of 600 s published previously [21,83], probably due to the presence of different small quantities of impurity. EuPO$_4$ possesses a short T_1 of 210 ms being close to that of the paramagnetic GdPO$_4$ (460 ms) [21]. For La$_x$Eu$_{1-x}$PO$_4$ ($x = 0.1, 0.2, 0.8, 0.9$), the T_1 values were determined for peaks 1–7 (low Eu^{3+}-content) and peaks 1–5 (high Eu^{3+}-content), as these peaks could easily be differentiated and possess similar shifts (Fig. 2, Table I, and Table S3). Peak 5, attributed to the P(La)$_7$(Eu)$_0$ units, possesses accordingly the longest T_1 compared to the other peaks, while being much shorter than the peak of neat LaPO$_4$. This confirms the presence of Eu^{3+} in the outer coordination sphere of such P atoms. Peaks 1 and 2 display the shortest T_1, a fact which also points toward a closer proximity to the paramagnetic cation as T_1 is proportional to r^6 according to the general equation [21,27,49,84,85]:

$$\frac{1}{T_1} = \frac{2}{5}\left(\frac{1}{4\pi}\right)^2 \frac{\gamma_P^2 g_e^2 \mu_B^2}{r^6} \langle S_z \rangle^2 \frac{3\tau_r}{1+\omega_P^2\tau_r^2} \qquad (2)$$

with γ_P being the phosphorus gyromagnetic ratio, g_e the electron g-factor, μ_B the Bohr magneton, r the Eu-P distance, $\langle S_z \rangle$ the thermal average of the z component of the electron spin, τ_r the electronic longitudinal relaxation time, and ω_P the ^{31}P Larmor frequency.

The shortest T_1 values indicate that peaks 1 and 2 might be, at first sight, respectively assigned to P1 and P2 for the P(La)$_6$(Eu)$_1$ units, as they possess the shortest Eu-P distance (Table S1). For $x = 0.8$, in a similar approach, the peaks at $\delta_{\text{exp}} \sim -5, 220,$ and 121 ppm might be attributed to P(La)$_7$(Eu)$_0$, and to P1 and P2 of P(La)$_6$(Eu)$_1$, respectively. We want to underline that this statement is made as a first approximation, as peak attribution solely based on T_1 is not always true [24]. For the two highest Eu^{3+}-content samples ($x = 0.1$ and 0.2), all peaks possess relatively similar and

short T_1 values, precluding an assignment from considerations on distances alone.

For the other compositions, as it was not straightforward to fit all peaks, the spectra were divided into three regions of $\delta_{\exp}$, the shifts ranges and T_1 values being specified in Table S2. R1 corresponds to species with shifts close to pure EuPO$_4$, R2 to species with $\delta_{\exp}$ in between pure EuPO$_4$ and LaPO$_4$ and R3 to species with shifts close to pure LaPO$_4$. T_1 is the shortest for the peaks belonging to R1 and R2 peaks have intermediate T_1 values and R3 the longest T_1 values. There is a slight T_1 increase with increasing La content as observed for La$_x$Nd$_{1-x}$PO$_4$ [21,22].

4. Temperature effects compared with La$_{0.99}$Nd$_{0.01}$PO$_4$

As previously done by Palke and Stebbins [14] for a lanthanum-neodymium orthophosphate with very low Nd^{3+} content, we also performed variable temperature experiments on the lowest Eu^{3+}-doped sample as it presents the best spectral resolution (Fig. S3 [61]). The peaks corresponding to the seven P sites surrounded by one Eu^{3+} and six La^{3+} cations gave the best resolution and are therefore the ones discussed here. Peaks 1, 2, 3, 6, and 7 have their positions affected by temperature. The range of paramagnetic shifts in the present study is much broader than the one observed for La$_{0.99}$Nd$_{0.01}$PO$_4$ and all peaks are more sensitive to temperature as illustrated by the sharper slopes (Fig. S4 [61]). The peaks with the highest positive paramagnetic shifts (peaks 1 and 2) have the most important temperature variations similarly to peaks A and B in the La$_{0.99}$Nd$_{0.01}$PO$_4$ spectrum (Fig. S4). Signals with positive paramagnetic shifts will move upfield while those with negative paramagnetic shifts will move downfield with increasing temperatures. We do not believe that these similarities are random and it might thus be possible that peaks A and B in the La$_{0.99}$Nd$_{0.01}$PO$_4$ spectrum correspond to the P1 and P2 sites, respectively. However, our suggestion is only speculative because no T_1 measurements were shown by Palke and Stebbins [14]. On the other hand, Maron *et al.* [21] published T_1 measurements on a La$_{0.90}$Nd$_{0.10}$PO$_4$ sample, but they only provided an average value over all peaks.

B. Prediction of the ^{31}P paramagnetic shifts

1. Pseudocontact and contact shifts

The formula for the experimental NMR shifts of a paramagnetic compound caused by a rare-earth center is [37,39,49]

$$\delta_{\exp} = \delta_{\mathrm{dia}} + \underbrace{\delta_{\mathrm{FC}} + \delta_{\mathrm{PC}}}_{\delta_p} \tag{3}$$

The anisotropic part of the shift by Eu^{3+} has been analyzed by Bleaney separately from the other rare-earth cations due to its nonmagnetic ground state ($J = 0$). He considered that the PC is only due to the anisotropy in the magnetic susceptibility, that the ELs are nondegenerate (original Van Vleck theory) and the excited states ($J = 1, 2,$ and 3) have to be considered [26,86].

The formula applied to calculate the δ_{PC} directly has been derived from Bleaney's theory and is currently the most

used [24,27,37,39,87]:

$$\delta_{\mathrm{PC}} = C_j B_0^2 \frac{3z^2 - r^2}{r^5} + \sqrt{6} C_j B_2^2 \frac{3x^2 - y^2}{r^5} \tag{4}$$

with C_j being a constant equal to 4 for Eu^{3+} (relative to -100 ppm for Dy^{3+}) calculated by Golding and Pyykkö [29] for LnCl$_3$ matrices with $B_0^2 = 274\,\mathrm{cm}^{-1}$ at 300 K [37,39]. C_j includes the excited states and the temperature dependency and is commonly applied for the Ln^{3+} series giving already successful results to calculate the δ_{PC} [37,39,85]. We will denote this approach as Golding and Pyykkö approach (GPA) in the following discussion.

Another formula has been determined by Bleaney [26] in its original theory and allows, to calculate the PC shieldings. The following equation for the PC with temperature dependency is [26]

$$\sigma_{\mathrm{PC}} = L\,F'' \left[\frac{1 - f(T)e^{-x}}{1 + 3e^{-x}} \right]. \tag{5}$$

The L constant is proportional to r^{-3} (r being the Eu-P radial distance) and to the $J = 1, 2, 3$ nondegenerate multiplets; F'' is a constant which depends on the radial angle θ, the polar angle φ, and the crystal field parameters B_2^0 and B_2^2; $f(T)$ is a temperature dependent function which includes the nondegenerated excited levels; finally $x = \frac{E_1}{k_B T}$ (where E_1 is the energy of the first excited state $J = 1$ in J, k_B the Boltzmann constant in J K^{-1} and T in K) is the classical Boltzmann distribution. All these terms are compiled in Table III. We will denote this approach as the Bleaney theory (BT) in the following discussion. By comparing the two formulas to retrieve δ_{PC} and the σ_{PC}, one can notice that for the shielding calculations all the parameters can be set and the use of a pre-calculated C_j constant—with CFP which might not correspond to our compound—is not necessary.

The isotropic part of the contact shift for a free ion has been calculated by some authors using the formula [23,30,37,39,88,89]:

$$\delta_{\mathrm{FC}} = \frac{A_{\mathrm{iso}}}{\hbar} \frac{\mu_B \langle S_z \rangle}{3\gamma_P k_B T} \times 10^6, \tag{6}$$

where $A_{\mathrm{iso}}/\hbar$ is the electron-nucleus transferred hyperfine coupling constant (in Hz, A_{iso} in J and $\hbar$ the inverse of the Planck constant in J s), $\langle S_z \rangle$ is the reduced value of the average spin polarization (no unit), γ_P is the gyromagnetic ratio of the observed nucleus ^{31}P (Hz T^{-1}), μ_B (J T^{-1} or A m^2), k_B is the Boltzmann constant, and T in K. However, more recent works [31–33] have shown that the g factor is missing from Eq. (7) and the correct expression is the following:

$$\delta_{\mathrm{FC}} = \frac{\mu_B \langle S_z \rangle}{3\gamma_P k_B T} \mathrm{tr}[\boldsymbol{g}\boldsymbol{a}_N] \times 10^6, \tag{7}$$

with $\boldsymbol{g}$ the g-tensor and $\boldsymbol{a}_N$ is the hyperfine coupling tensor of the probe nucleus. The value of the g-tensor is obtained from $g = g_e + \Delta\boldsymbol{g}$ with $g_e = 2.0023$ [63].

As the empirical formulas for both the PC and FC shifts include temperature dependence, the variation of peaks position with increasing temperatures can now be understood.

TABLE III. The terms C, F″ and $f(T)$ are used to calculate the σ_{PC} based on the original Bleaney's theory [26] as discussed in the text. μ_B is the Bohr's magneton (in J T^{-1}), μ_0 the permeability in vacuum (in T m A^{-1}), r^{-3} the Eu-P distance (in Å), E_1, E_2, and E_3 the energies of the $J = 1, 2,$ and 3 nondegenerate energy levels (in J), B_2^0 and B_2^2 the CF parameters (in J), and σ_2 the screening coefficient equal to 0.52 [90,91].

L	F''	$f(T)$
$\frac{4\mu_B^2\mu_0}{E_1^2 4\pi r^3}\left(1 + \frac{2E_1}{E_2}\right)$	$\left[2 \times \frac{B_2^0}{1-\sigma_2}(3\cos^2\theta - 1) + 2\frac{B_2^2}{1-\sigma_2}(\sin^2\theta\cos2\varphi)\right]$	$\left\{\frac{1}{(1+\frac{2E_1}{E_2})}\right\}\left\{1 + \frac{2E_1}{E_2-E_1} - \frac{E_1^2}{2(E_2-E_1)^2}\right.$ $\left. - \frac{3E_1^2}{(E_2-E_1)(E_3-E_1)}\right.$ $\left. + x\left(1 + \frac{15E_1}{16(E_2-E_1)}\right) + \frac{9}{32}x^2\right\}$

C. Energy levels and crystal field parameters

It is clear from the previous part that in order to predict the δ_{PC}, prior knowledge of the energy levels and CFP is required. To do so, we determined the energy levels *a)* by fitting the experimental $\chi_{mol.Eu3+}$ curves using the free ion approach and *b)* with theoretical calculations performed for La$_{0.9}$Eu$_{0.1}$PO$_4$.

1. The low-temperature upturn

This type of upturn was observed in several other Eu^{3+}-based materials [78,92–96]. While some authors attributed it to the presence of Eu^{2+} impurities [78], others excluded this +2 oxidation state. Indeed, by combining magnetic susceptibility measurements with ^{151}Eu Mössbauer spectroscopy, no Eu^{2+} signal could be detected [92,97–99] while its contribution is usually easily detected [80,100,101].

XPS is also very powerful to discriminate between these two oxidation states [102–104], as it is a high-sensitive surface technique facilitating a detection down to one atomic percent. Thus the La$_{0.1}$Eu$_{0.9}$PO$_4$ sample has been characterized by XPS as it contains the highest Eu content. The spectra are presented in Fig. S7 [61]. First the Eu-4d line was considered. The 4d photoemission lines of Eu^{2+} appear at about 9.3 eV lower binding energy (BE) than the lines of Eu^{3+} for several binary compounds (Eu-O, Eu-F) [103]. The received sample does not show any intensity that could be attributed to Eu^{2+}. The peak at 132.2-eV BE, attributed to P-2p, is separated by 3 eV from the Eu$_{4d5/2}$ line. To completely exclude its possible assignment to Eu^{2+} (4d-5/2), we exposed the surface to atomic oxygen at room temperature—which would oxidize surface Eu^{2+} to Eu^{3+}. There was no spectral modification, which is consistent with the P-2p nature of this peak or the exclusive presence of Eu^{2+} in the sample. Finally, the Eu-3d spectrum shows the presence of the Eu^{3+}-3d peaks and the absence of Eu^{2+}-3d (which would also appear shifted to 9 eV lower BE than the Eu^{3+} peaks). The present analysis clearly excludes the Eu^{2+} cation as the cause of this low-temperature upturn on the magnetic susceptibility curves. It is worth mentioning that it is difficult to obtain neat Eu^{3+} and that as other rare-earth ions might be also present, they can be the cause of this low-temperature upturn. Another hypothesis to this low-temperature upturn, which is more important for the La$_{0.9}$Eu$_{0.1}$PO$_4$ sample, would be a slight effect of the diamagnetic contribution as observed for LaPO$_4$.

2. Fitting with the free Eu^{3+} ion model

Due to its electronic configuration, Eu^{3+} possesses a diamagnetic ground state, and it is the mixing with the excited states which leads to the peculiar Van Vleck paramagnetism [81,82,105,106]. In the case of a free Eu^{3+} ion, all the energy levels are nondegenerate and the magnetic susceptibility can be fitted using a pure VV interaction following the equation [78]:

$$\chi_{VV} = \left(\left(N_A\mu_B^2\right)\Big/\left(1 + 3\exp\left(-\frac{\lambda}{T}\right) + 5\exp\left(-\frac{3\lambda}{T}\right) + 7\exp\left(-\frac{6\lambda}{T}\right) + 9\exp\left(-\frac{10\lambda}{T}\right) + 11\exp\left(-\frac{15\lambda}{T}\right)\right.\right.$$
$$\left.+ 13\exp\left(-\frac{21\lambda}{T}\right)\right) \times \left(24 + \left(13.5\left(\frac{\lambda}{T}\right) - 1.5\right)\exp\left(-\frac{\lambda}{T}\right) + \left(67.5\left(\frac{\lambda}{T}\right) - 2.5\right)\exp\left(-\frac{3\lambda}{T}\right)\right.$$
$$\left.+ \left(189\left(\frac{\lambda}{T}\right) - 3.5\right)\exp\left(-\frac{6\lambda}{T}\right) + \left(405\left(\frac{\lambda}{T}\right) - 4.5\right)\exp\left(-\frac{10\lambda}{T}\right) + \left(742.5\left(\frac{\lambda}{T}\right) - 5.5\right)\exp\left(-\frac{15\lambda}{T}\right)\right.$$
$$\left.\left.+ \left(1228.5\left(\frac{\lambda}{T}\right) - 6.5\right)\exp\left(-\frac{21\lambda}{T}\right)\right)\Big/\left((3\lambda k_B) 10^{-1}\right)\right). \tag{8}$$

In this approach (called thereafter model 1), the only variable is the λ parameter which corresponds to the energy of the first excited state (E_1). E_1 is related to the other energy levels as shown in the diagram in Fig. S8 [61]. The best fit parameters of λ [Fig. 3(b)] are reported in Table II. The susceptibility curves were fitted limiting the space to the lowest three multiplets ($J = 0, 1, 2$), since the inclusion of further excited states did not improve the quality significantly. Similarly, releasing the constraint between the energy levels ($E_1 = 3E_2 = 6E_3$) did not improve the fits. While model 1 properly describes the low-temperature VV constant behavior important for setting the energy level values, it does not

reproduce the very low-temperature upturn previously discussed. Therefore the curves were also fitted using model 2 which includes the upturn in the fit by adding a scaled Curie-Weiss law to the Van Vleck paramagnetism formula (VVCW) using the following equation:

$$\chi_{\text{VVCW}} = f_i \frac{C}{T - \theta_p} + (1 - f_i)\chi_{\text{VV}} \qquad (9)$$

with f_i being the percentage of paramagnetic impurities leading to a CW behavior, C the Curie-Weiss constant, and θ_p the Weiss temperature. Some authors proceeded similarly to fit their curves [92]. There is now a better fit of the global magnetic susceptibility curves, especially for La$_{0.9}$Eu$_{0.1}$PO$_4$.

3. Theoretical calculations for the La$_{0.9}$Eu$_{0.1}$PO$_4$ sample

Using the following approach, denoted thereafter as Model 3, it was possible to determine both the energy levels and the CFP (B_k^q, A_k^q). As such crystal field calculations are limited to a magnetic center completely isolated from other magnetic ions, we focused on the sample with the lowest Eu-content. The full set of CFP has been determined using the REC [56] model in the SIMPRE computational package [55]. As the energy level fitting in the SIMPRE code is limited to the ground J multiplet being $J = 0$ for Eu^{3+}, we took advantage of the spectroscopic energy levels reported for the isostructural NdPO$_4$ derivative [107] [$J(\text{Nd}^{3+}) = 9/2$]. This allowed us to obtain the REC parameters that model the crystal field effect

of the phosphonate ligands ($D_r = 0.749$ Å and $Z_i = 0.371$). Then, we applied them to the experimental coordinates of La$_{0.9}$Eu$_{0.1}$PO$_4$ in order to calculate the 27 CFP using the following expressions:

$$A_k^0 = \frac{4\pi}{2k+1} \sum_{i=1}^{N} \frac{Z_i e^2}{R_i^{k+1}} Z_{k0}(\theta_i, \varphi_i) p_{kq}, \qquad (10)$$

$$A_k^q = \frac{4\pi}{2k+1} \sum_{i=1}^{N} \frac{Z_i e^2}{R_i^{k+1}} Z_{kq}(\theta_i, \varphi_i) p_{kq} \ (q > 0), \qquad (11)$$

$$A_k^q = \frac{4\pi}{2k+1} \sum_{i=1}^{N} \frac{Z_i e^2}{R_i^{k+1}} Z_{k|q|}(\theta_i, \varphi_i) p_{k|q|} \ (q < 0), \qquad (12)$$

where R_i, θ_i, and φ_i are the effective polar coordinates of the point charges; Z_i is the effective point charge, associated to the ith donor atom with the lanthanide at the origin; N is the number of ligands; e is the electron charge; p_{kq} are the prefactors of the spherical harmonics and Z_{kq} are the tesseral harmonics expressed in terms of the polar coordinates for the ith donor atom. The full set of EL and CFP are given in Tables S4 and S5 [61].

In order to obtain the energy levels and the magnetic susceptibility curve of the system, the calculated CFP were introduced into the CONDON package that uses the following full Hamiltonian:

$$\hat{H}_{\textbf{Full}} = \underbrace{\sum_{i=1}^{N}\left[-\frac{\hbar^2}{2m_e}\nabla_i^2 + V(r_i)\right]}_{\hat{H}_0} + \underbrace{\sum_{i>j}^{N}\frac{e^2}{r_{ij}}}_{\hat{H}_{ee}} + \underbrace{\sum_{i>j}^{N}\boldsymbol{\xi}(r_i)\kappa\widehat{\mathbf{l}}_l \cdot \hat{\mathbf{s}}_i}_{\hat{H}_{SO}}$$

$$+ \underbrace{\sum_{i=1}^{N}\sum_{k=2,4,6}\sum_{q=1}^{k}\left\{B_k^q\left[C_k^{-q}(i) + (-1)^q C_k^q(i)\right] + iB_k^q\left(C_k^{-q}(i) - (-1)^q C_k^q(i)\right)\right\}}_{H_{CF}} + \underbrace{\sum_{i>j}^{N}\mu_B\left(\kappa\widehat{\mathbf{l}}_l + g_e\hat{\mathbf{s}}_i\right)\cdot\mathbf{B}}_{\hat{H}_{mag}}, \qquad (13)$$

where $\hat{H}_0$ represents the energy in the central field approximation (which is neglected), $\hat{H}_{ee}$ the interelectronic repulsion, $\hat{H}_{CF}$ the crystal field with C_k^q the spherical tensors, $\hat{H}_{so}$ the spin-orbit coupling, and $\hat{H}_{mag}$ the Zeeman effect of an external magnetic field $\mathbf{B}$. The calculated magnetic susceptibility is finally plotted with the experimental one in Fig. 3(c) showing how well such an approach is able to reproduce the experimental data. With model 3, the values of the degenerate EL (J up to 4) can now be determined, which was not possible with the free ion approach.

The B_2^0 and B_2^2, which are of interest for the δ_{PC} calculations, are also compared with the experimentally determined ones for an LaPO$_4$ matrix doped with low Eu^{3+}-content and the ones determined by Antic-Fidancev *et al.* [107] (see Table IV). The agreement is remarkable considering that the previous works assumed an axial C_{2v} symmetry around the Eu^{3+} cation (this approximation often done for other rare earths [108,109]) while we used experimental coordinates.

4. Comparison of the energy levels

As the energy level values determined with the free ion approach (Models 1 and 2) are expressed in kelvin in the CGS system of unit (magnetic susceptibility being expressed in emu mol^{-1}) [78], they have been converted in cm^{-1} as it is the unit which is employed most of the time (the SI unit being the Joules). Independently of the model considered, using the free ion approach, the values are in good agreement with the $^7F_1$ EL equal to 379 cm^{-1} for the free Eu^{3+} ion

TABLE IV. Calculated crystal field parameters.

	B_2^0 (cm^{-1})	B_2^2 (cm^{-1})
La$_{0.9}$Eu$_{0.1}$PO$_4$ (this work)	−623	71
1% − 5%-Eu^{3+} LaPO$_4$ (Antic-Fidancev [107])	−649 (23)	129 (13)
EuPO$_4$ [110]	−707 (9)	−62 (4)

[81]. The λ values (Table II) between models 1 and 2 are not very different ($\sim 30 \, \text{cm}^{-1}$) meaning that both approaches are equivalent in describing the EL. While a better fit is obtained with Model 2, the physics behind the constants C and θ_p can be questioned. Indeed, the meaning of the Curie constant, which is characteristic of the effective magnetic moment, gives incoherent values (Table II) in the way that, effective moments equal to 0.1 and 0.2 can be calculated for $EuPO_4$ and $La_{0.9}Eu_{0.1}PO_4$, respectively. These peculiar values exclude the presence of Eu^{2+} cations as an impurity ($\mu_{\text{eff}} = 7.94 \, \mu_B$) and might be attributed to a mixing of several rare-earth paramagnetic cations. Also, the percentage of paramagnetic impurity leading to this upturn is very small (Table II). Overall, considering Model 1 or 2, there is an increase of the EL values with increasing La content. To compare this evolution with the one obtained theoretically, we have to suppose that the energy levels are also nondegenerate (average value of the three calculated M_S levels for $J = 1$). Accordingly, for the low Eu^{3+} content, $^7F_1 = 391.2 \, \text{cm}^{-1}$ was determined. For $EuPO_4$, calculations of the EL were previously done [76] (Table S4) and a $^7F_1 = 371 \, \text{cm}^{-1}$ was deduced. These higher theoretical values compared to those determined using the free ion approach are not surprising as the full Hamiltonian is now considered. Overall, there is always a decrease of the EL with increasing Eu^{3+} content independently from the model used.

D. Calculations of the EPR parameters using cluster models

In these calculations, we modelled the Eu^{3+} dilution in a diamagnetic matrix, i.e., the effect of a single Eu^{3+} ion on the NMR shift of ^{31}P. To predict the δ_{FC} [Eqs. (7) and (8)], we need A_{iso} or $\text{tr}[\boldsymbol{ga}_N]$. They can be determined by DFT calculations on an appropriate model structure containing one P atom surrounded by six La^{3+} cations and one paramagnetic center. Unfortunately, due to its nonmagnetic ground state, the calculation of EPR parameters using DFT calculations for the Eu^{3+} cation is not straightforward. However, a team of researchers [37–39] overcame this drawback by substituting this $4f^6$ cation by Gd^{3+} ($4f^7$). They multiplied the obtained A_{iso} values by a factor of 0.34 and succeeded in predicting the paramagnetic shifts. Luckily in our case, the $La_xGd_{1-x}PO_4$ [21,111] system still belongs to the monazite series and thus this approach can be used.

Hence, we relaxed the $LaPO_4$ crystalline structure using the QUANTUM ESPRESSO software (details in the Experimental Part). Then, the full structure was approximated by cluster models. Recent results [112,113] on $3d$-element-based materials (Mn, Fe, Co, Ni) showed that the paramagnetic shifts were similarly well reproduced using the cluster model approach as by solid-state calculations. To render the local environment effects on the EPR parameters, we considered two cluster models presented in Fig. 4.

In the C1 model structure with the molecular formula of $P_1La_6Gd_1O_{25}H_{21}$ the P atom is in the center surrounded by four O atoms as the first coordination sphere. Seven Ln (Ln = La, Gd) atoms form the second coordination sphere. The fixed coordinates of these atoms correspond to the APO structure. The outer coordination sites of the Ln atoms (third coordination sphere) are terminated by relaxed OH groups. The cluster has a charge of $-3 \, e$. In this model the surrounding
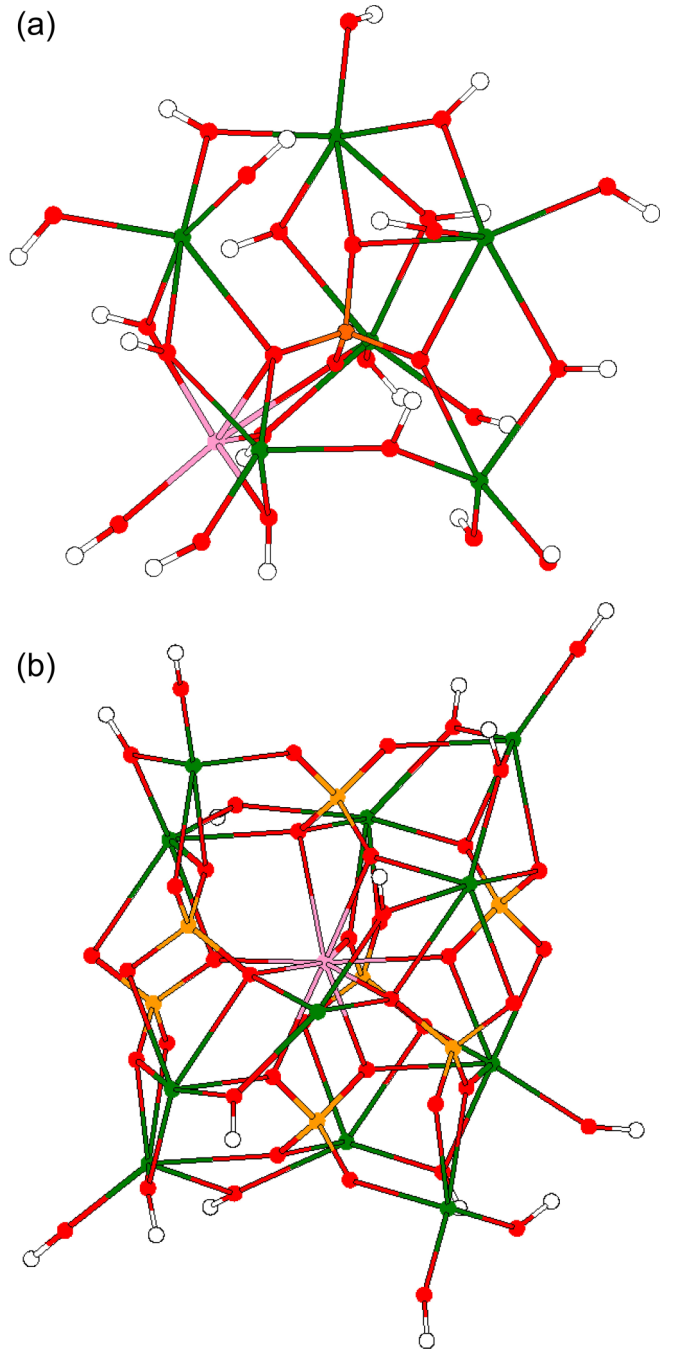

FIG. 4. Model structures used for the calculations of the isotropic hyperfine coupling constants: (a) the $P_1Gd_1La_6O_{25}H_{21}$ cluster C1 (considering here P2 as the central atom) and (b) the $Gd_1P_7La_{11}O_{40}H_{11}$ cluster C2. The following color code is used: La atoms are in green, P atoms in orange, Gd atoms are in pink, H atoms are in white, and O atoms in red. In the insert, the local environment around the P atom is presented.

of the central P atom corresponds to that in the crystal, therefore it is described very well. The description of the Ln atoms in the second coordination sphere, however, may somewhat suffer from the replacement of the crystal O atoms by relaxed OH groups. In order to account for the seven magnetically different environments; seven C1 clusters were implemented substituting each time a different La^{3+} atom

TABLE V. Isotropic hyperfine coupling constants ($A_{\rm iso}/\hbar$, MHz) and shifts due to the Fermi contact interaction ($\delta_{\rm FC}$, ppm) calculated based on the P$_1$La$_6$Gd$_1$O$_{25}$H$_{21}$ (C1) and Gd$_1$P$_7$La$_{11}$O$_{40}$H$_{11}$ (C2) clusters. As suggested previously [37–39], the $A_{\rm iso}/\hbar$ values determined from the Gd^{3+} clusters were scaled by a factor of 0.34 in order to predict the ones expected for an Eu^{3+} cluster.

P site	$A_{\rm iso}/\hbar$	$\delta_{\rm FC1}$ (C1)	$A_{\rm iso}/\hbar$	$\delta_{\rm FC2}$ (C2)	tr[$g a_N$]	$\delta_{\rm FC3}$ (C2)
P1	0.177	73.4	0.166	69.1	0.599	248.8
P2	0.129	53.8	0.107	44.6	0.382	158.7
P3	0.061	25.3	0.043	18.0	0.173	71.9
P4	0.017	7.2	0.016	6.5	0.060	25.0
P5	−0.012	−4.97	−0.016	−6.7	−0.059	−24.5
P6	−0.015	−6.2	−0.003	−1.1	−0.001	−0.5
P7	−0.041	−16.9	−0.017	−7.1	−0.059	−24.7

by a Gd^{3+} atom. The calculated $A_{\rm iso}/\hbar$ values are given in Table V. For P1 and P2, possessing the highest $A_{\rm iso}/\hbar$ values, we tested the larger QZ4P-J basis set in order to see how it influences this parameter. Very similar values of 0.170 and 0.123 MHz, respectively, were obtained. This shows that, in the present case, the TZ2P-J basis set is good enough for this parameter.

To better describe the local environment around the Gd atom, we implemented the cluster C2 model with the molecular formula of Gd$_1$P$_7$La$_{11}$O$_{40}$H$_{11}$. It contains a Gd^{3+} atom in the center surrounded by seven PO$_4$ groups as the first coordination sphere. The second coordination sphere consists of eleven La atoms. The fixed coordinates of these atoms correspond to the APO structure. The outer coordination sites of the La atoms are terminated by relaxed OH groups. The cluster has a charge of 0 e. In this model, the surrounding of the central Gd atom corresponds to that in the crystal, therefore it is described very well. The description of the P atoms in the second coordination sphere should be also very good, because they are surrounded with O atoms and at a further distance by the closest La atoms, exactly as in the crystal structure. On the other hand, the description of the outer La atoms may somewhat suffer from the replacement of the crystal O atoms by relaxed OH groups. Due to the better description of Gd and the P atoms, the C2 model should be superior to C1. Using this C2 model, the $A_{\rm iso}/\hbar$ values of the seven P sites could conveniently be obtained in one calculation (Table V). One can observe that the two sets of $A_{\rm iso}/\hbar$ values from the C1 and C2 model structures are quite similar except for P6 and P7.

In addition, using the C2 model, we calculated also the a_N and g tensors and from them evaluated the g-factor by matrix operations. The obtained value of 1.236 is much lower than the experimental g-factor of 1.995 [111]. We therefore do expect that this approach will lead to important uncertainties.

E. Nature and prediction of the ^{31}P paramagnetic shifts

1. The LnPO$_4$ series (Ln = La, Ce, Pr, Nd, Sm, and Eu)

In order to understand the origin of the paramagnetic shift in EuPO$_4$, we considered the ^{31}P $\delta_{\rm exp}$ for the given series as was previously done for other crystalline phases [20,50,52]. Thus the $\delta_{\rm exp}$ data recorded at 31.25 kHz by Bregiroux *et al.*
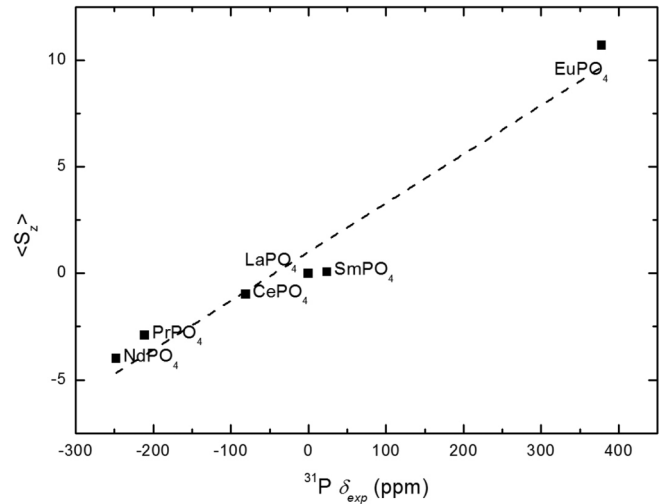

FIG. 5. Variation of the ^{31}P $\delta_{\rm exp}$ obtained by Bregiroux *et al.* [19] at 31.25 kHz against the average electron spin polarization $\langle S_z \rangle$ determined by Golding and Halton [30] for the LnPO$_4$ (Ln = La − Eu) series. The dashed line is a linear correlation with an adjusted coefficient of 0.95.

[19] were plotted against the average electron spin polarization $\langle S_z \rangle$ values calculated by Golding and Halton [30] in Fig. 5. A good linear correlation is observed through the series suggesting a constant $A_{\rm iso}$ in contrast to previous results [20]. As the $\delta_{\rm exp}$ data were determined from static conditions [20], this difference might be linked with higher uncertainties on the NMR shifts in such conditions. This linear relation also shows that the Fermi contact interaction is the dominant one. Furthermore, by plotting the $\delta_{\rm exp}$ against the C_j parameters calculated by Golding and Pyykkö [29], we can attribute the variation of the paramagnetic shifts to the PC interaction. Here, as shown in Fig. S9 [61], we did not obtain a linear correlation, excluding any significant role of this interaction in the variation of the shifts.

2. La$_{0.1}$Eu$_{0.9}$PO$_4$

The $\delta_{\rm PC1}$ and $\sigma_{\rm PC1}$ data were calculated for this rich Eu^{3+}-doped solid solution using the CFP previously determined in pure EuPO$_4$ [110] and the energy levels published by Bronova *et al.* [76]. The atomic coordinates required for the calculations [Eq. (5), Eq. (6), and Table III] are those from EuPO$_4$. The calculated values are presented in Table VI. As expected, the $\sigma_{\rm PC1}$ and the $\delta_{\rm PC1}$ values possess opposite signs. As the same interaction acts for the shielding and the shift, we considered that a linear relation exists between these two parameters following the equation $\delta_{\rm PC2} = a.\sigma_{\rm PC1}$ (with a as the scaling factor). This rescaling was previously applied by Bleaney *et al.* [86] and gave good results. The two approaches provided similar pseudocontact shift values ($\delta_{\rm PC1}$ and $\delta_{\rm PC2}$, cf. Table VI). It is interesting to notice that the $\delta_{\rm PC}$ values (with similar signs) determined for the different P sites have very close values. This might be a good explanation for the fewer signals (due to overlapping) in this rich Eu^{3+}-doped sample. However, these empirically calculated shifts are very different from the experimental δ_p(exp) ones. It is clear that, for this sample, the PC interaction is not the only one responsible for

TABLE VI. Calculated pseudocontact shieldings, σ_{PC} (in ppm), and pseudocontact shifts δ_{PC} (in ppm) determined with the CFP and EL from the present study (PS), from Antic-Fidancev *et al.* [107] (AF), and independently by Chen [110] *et al.* and Bronova *et al.* [76] (CB). The Bleaney theory (BT) or Golding and Pyykkö approach (GPA) were used for their prediction.

| | La$_{0.1}$Eu$_{0.9}$PO$_4$ | | | La$_{0.9}$Eu$_{0.1}$PO$_4$ | | | | | |
| | δ_{PC1}, GPA | σ_{PC1}, BT | δ_{PC2}, BT | δ_{PC3}, GPA | | σ_{PC2}, BT | | δ_{PC4}, BT | |
	CB			PS	AF	PS	AF	PS	AF
P1	92.1	−476.9	85.9	53.2	39.3	−388.7	−363.9	64.2	62.1
P2	87.3	−455.9	82.1	48.1	35.5	−351.9	−329.3	58.1	56.2
P3	45.3	−309.3	55.7	70.8	84.1	−373.7	−412.0	61.7	70.4
P4	−45.8	253.8	−45.7	−12.6	−9.4	91.2	85.6	−15.0	−14.6
P5	−48.8	295.7	−53.3	−74.6	−77.8	442.5	458.6	−73.0	−78.3
P6	35.1	−244.2	44	50.6	60.6	−264.2	−292.8	43.6	50.0
P7	−48.3	271.2	−48.9	−27.4	−26.8	170.8	172.7	−28.2	−29.5

the experimental shifts and that FC, which is the dominant interaction in EuPO$_4$, contributes probably in a substantial degree. This may also be the source of the different behavior: the calculated δ_{PC} values change sign for some P sites while all the experimental peaks with relative intensities $\geqslant 4\%$ have positive δ_p(exp) shifts. Unfortunately, it was not possible to predict the FC interaction by determining the A_{iso} using an appropriate model structure for La$_{0.1}$Eu$_{0.9}$PO$_4$, as our DFT calculations failed for structures containing more than one Ln with unpaired electrons.

3. La$_{0.9}$Eu$_{0.1}$PO$_4$

Based on Eqs. (5)–(8), we attempted to attribute the different signals of the P(La)$_6$(Eu)$_1$ units by calculating theoretically the paramagnetic shifts and comparing them with the experimental paramagnetic shifts, δ_p (exp). In order to obtain δ_p(exp), we subtracted the diamagnetic contribution (δ_{dia}, the shift corresponding to the P(La)$_7$ units, i.e., the unshifted peak at −4.5 ppm) from the experimental shifts, δ_{exp}, following the equation δ_p(exp) $= \delta_{exp} - \delta_{dia}$ [14,37,39,44,114] (Table I). Then, to calculate empirically the pseudocontact shift based on the Golding and Pyykkö approach, δ_{PC3} [Eq. (5)], and the paramagnetic shielding based on Bleaney's theory, σ_{PC2} [Eq. (6)], we used the theoretical CFP and EL values evaluated in the present study (PS) and compared the results with those previously published by Antic-Fidancev (AF) *et al.* [107]. Like δ_p (exp), four P sites have positive calculated $\delta_{PC3}/\sigma_{PC2}$ values (Table VI) and three others have opposite signs. By comparing δ_{PC3} determined using the two sets of CFP and EL (Table VI, Fig. S10(a) [61]), one can notice a difference of $\sim 20\% - 25\%$ (in relative intensity) for P1, P2, P3, P4, and P6; while for the σ_{PC2} this difference is less significant reaching max. $\sim 11\%$ for P6. As previously described, the σ_{PC2} data have been rescaled based on δ_{PC3} (similarly to reference 83) to obtain the δ_{PC4} values. Very close scaling factors of −6.04 and −5.85 were determined using the CFP and EL data from the PS and AF works, respectively. As the pseudocontact shifts determined with the CFP and EL from the present study give more coherent results, we will focus our discussion on these values. Both approaches (i.e., BT and GPA), give differences up to $\sim 17\%$, the minimum differences obtained for P5 (2%) and P7 ($\sim 3\%$) [Fig. S10(b)].

As the FC interaction is missing from these calculations, the theoretical FC shifts, δ_{FC}, were separately calculated taking advantage of the "dilution" of a paramagnetic cation in a diamagnetic matrix. To do so, the reduced value of the average spin polarization parameter $\langle S_z \rangle$ needs to be determined, as expressed by Eqs. (7) and (8). Then, assuming a Boltzmann distribution, this parameter can be obtained using the following equation [115]:

$$\langle S_z \rangle = \frac{\sum_J \langle S_z \rangle_J (2J+1) \exp\left[-E_J J(J+1)/2kT\right]}{\sum_J (2J+1) \exp\left[-E_J J(J+1)/2kT\right]} \quad (14)$$

and

$$\langle S_z \rangle_J = \frac{(g-\gamma)gJ(J+1)}{(2-\gamma)} + \frac{(2kT/E_J)(g-\gamma)(g-2)}{(2-\gamma)}$$

with E_J being the energy level of the J states. Also, similarly to Pinkerton *et al.* [115], we set g the Landé g factor to 4.4, the γ orbital reduction factor to 1, while the k Boltzmann constant is equal to 0.695 cm^{-1}/K. A $\langle S_z \rangle$ value of 10.56 has been determined at 334 K (the temperature corresponding to the experimental conditions). This value is really close to the $\langle S_z \rangle = 10.68$ value, determined previously by Golding and Pyykkö [29].

Using the two sets of A_{iso} values and the tr[ga_N] product obtained in our cluster model calculations (vide supra), three sets of paramagnetic shifts due to the Fermi Contact interaction were determined (Table V). By comparing δ_{FC} determined using Cluster 1 (δ_{FC1}) to those from Cluster 2 (δ_{FC2}), large differences were obtained for P6 ($\sim|82|\%$) and P7 ($\sim|58|\%$), originating from the largely different A_{iso} values. It is also noteworthy that, both Fermi contact shifts are of highest importance for P1 and P2, which possess the shortest distances to the paramagnetic center. This observation seems to comfort the previous statement based on T_1. As expected, δ_{FC3} present different and larger values of shifts than both δ_{FC1} and δ_{FC2}.

Finally, in Table VII, the theoretical paramagnetic shift values are shown as determined by summing the pseudocontact shifts (δ_{PC3} and δ_{PC4} in Table VI) with the Fermi contact shifts (δ_{FC1}, δ_{FC2}, and δ_{FC3} in Table V). The experimental and theoretical paramagnetic shifts are compared in Fig. 6. We first compare δ_{p1} with δ_{p2}, δ_{p3} with δ_{p4} and, δ_{p5} with

TABLE VII. Theoretically calculated paramagnetic shifts δ_p.

P site	$\delta_{p1} = \delta_{FC1} + \delta_{PC3}$	$\delta_{p2} = \delta_{FC1} + \delta_{PC4}$	$\delta_{p3} = \delta_{FC2} + \delta_{PC3}$	$\delta_{p4} = \delta_{FC2} + \delta_{PC4}$	$\delta_{p5} = \delta_{FC3} + \delta_{PC3}$	$\delta_{p6} = \delta_{FC3} + \delta_{PC4}$
P1	136.7	125.8	133.2	122.3	313.0	302.0
P2	111.2	101.3	102.6	92.7	216.8	206.8
P3	86.7	95.8	79.7	88.8	133.56	142.7
P4	−7.9	−5.4	−8.5	−6.0	9.9	12.4
P5	−77.9	−79.5	−79.8	−81.4	−97.6	−99.2
P6	37.4	44.4	42.5	49.4	43.1	50.0
P7	−44.9	−44.1	−35.3	−34.5	−52.9	−52.1

δ_{p6}(Fig. S11(a) [61]) to render the effect of replacing δ_{PC3} with δ_{PC4}. For most P sites, there are only small differences (up to ∼20%) between the two paramagnetic shifts except for P4 (up to ∼40%) probably because for this site there is a small theoretical paramagnetic shift value. Next, by fixing the PC shifts and changing the FC approach based on Eq. (7), one can note that the type of cluster model influences the paramagnetic shifts only moderately with differences up to ∼30% for P7 [Fig. S11(b)]. Also, independent from the type of cluster model used, the theoretical paramagnetic shifts values (considering δ_{FC1} and δ_{FC2}) are underestimated with respect to the experimental ones for P1, P2, and P4, while they are overestimated for the other P sites. At last, by using Eq. (8) to calculate δ_{FC3} (Fig. 6), there is an overall overestimation with respect to the experimental paramagnetic shifts values. This observation is not surprising, as the g-tensor might not be very well predicted underlining the rough approximation character of substituting Eu^{3+} to Gd^{3+}. Yet, there is a similar trend in the shifts based on the experiment and the two other theoretical approaches. This implies that it may still be a helpful approach for helping in the assignment of the different sites in a solid sample based on the overall trend.

Thus, we note that compared to the most recent works on calculated paramagnetic shifts for solid-state materials
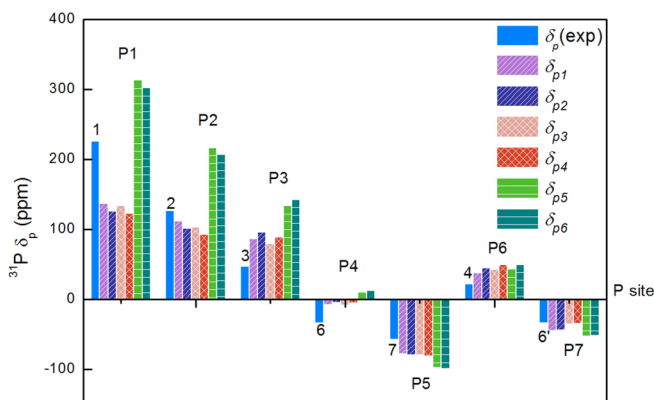

FIG. 6. Comparison between the experimental [δ_p(exp)] and theoretical paramagnetic shifts (δ_p) determined using Eq. (3). The peak numbers refer to δ_p(exp). The theoretical paramagnetic shifts are obtained by summing the pseudocontact shifts determined using the Golding and Pyykkö Approach (δ_{PC3}) or the Bleaney Theory (δ_{PC4}) with the Fermi contact shifts (FC) determined using cluster1 (δ_{FC1}), cluster 2 (δ_{FC2}), or by including the g-tensor approach (δ_{FC3}). More details are given in Table VII.

(mostly on $3d$ metals) using state-of-the-art DFT methods [112,113], the agreement between the present experimental and theoretical shifts is still very good. Moreover, whatever methods used, we obtained a clear trend allowing us to assign the NMR peaks unambiguously. Considering the numerous approximations needed because of the specific ground state of Eu^{3+} (namely, using Nd^{3+} to calculate CFP and EL, the cluster models and Gd^{3+} substituted to Eu^{3+}), it is quite encouraging to observe such trends and to achieve the distinction and attribution of each P(La)$_6$(Eu)$_1$ unit.

V. CONCLUSION

We have recorded ^{31}P MAS NMR spectra and magnetic susceptibility curves for a series of La$_x$Eu$_{1-x}$PO$_4$ solid solutions. The spectra of the Eu-containing samples are complex due to the paramagnetic character of Eu^{3+}: instead of a single peak expected from the unique crystallographic P site, several signals attributed to magnetically inequivalent P sites were detected. For the spectrum of La$_{0.9}$Eu$_{0.1}$PO$_4$, for example, we identified (i) one peak belonging to the P(La)$_7$ units, (ii) seven peaks with equivalent intensities for the P(La)$_6$(Eu)$_1$ units, and (iii) remaining intensities corresponding to the twenty one peaks belonging to the P(La)$_5$(Eu)$_2$ units.

We measured the T_1 relaxation time over the whole range of composition. The obtained faster longitudinal relaxation upon increase of the paramagnetic cation concentration facilitated the attribution of peaks 1 and 2 to the P1 and P2 sites, respectively, in the La$_{0.9}$Eu$_{0.1}$PO$_4$ and La$_{0.8}$Eu$_{0.2}$PO$_4$ spectra.

We were also able to better understand the magnetic properties by recording magnetic susceptibility curves for LaPO$_4$, La$_{0.9}$Eu$_{0.1}$PO$_4$, La$_{0.5}$Eu$_{0.5}$PO$_4$, and La$_{0.1}$Eu$_{0.9}$PO$_4$ and comparing them to the one previously published for EuPO$_4$. We observed the Van Vleck behavior for all the composition having paramagnetic Eu^{3+} cations. LaPO$_4$ displays a diamagnetic behavior. By fitting empirically the $\chi_{mol.Eu3+}$ using the free ion model, we extracted the nondegenerate energy levels. Furthermore, for La$_{0.9}$Eu$_{0.1}$PO$_4$, it was possible to fit theoretically the curve and predict the energy levels and crystal field parameters. Overall, there was a decrease of the EL values with increasing La^{3+} content.

The so-obtained energy levels and CFP allowed us to predict the pseudocontact shifts for both La$_{0.1}$Eu$_{0.9}$PO$_4$ and La$_{0.9}$Eu$_{0.1}$PO$_4$ using the BT and GPA methods for the P(La)$_6$(Eu)$_1$ units. We found that the use of the C_j constant gave δ_{PC} more dependents on the energy levels and crystal field parameters. These calculations confirmed that

this interaction plays an important role in the shifts, but the FC interaction has also to be considered. The Fermi contact shifts for a P atom surrounded by one paramagnetic cation were evaluated from theoretical EPR parameters obtained by DFT calculations. The diamagnetic electronic ground state of Eu^{3+} was circumvented substituting Eu^{3+} by the Gd^{3+} ion. Nonetheless, as expected, some differences have been observed between experimental and theoretical shifts due to these approximations. Thanks to a similar trend in the shifts, it has yet been possible to assign each signal of the $P(La)_6(Eu)_1$ units, and on its basis to achieve the interpretation of the $La_{0.9}Eu_{0.1}PO_4$ spectrum.

As these crystalline phases are also considered as matrices for radioactive materials, we plan to use the same approach on similar matrices doped with actinide cations.

[1] N. Dacheux, N. Clavier, and R. Podor, Versatile Monazite: Resolving geological records and solving challenges in materials science: Monazite as a promising long-term radioactive waste matrix: Benefits of high-structural flexibility and chemical durability, Am. Mineral. **98**, 833 (2013).

[2] R. C. Ewing, W. Weber, and F. Clinard, Radiation Effects in nuclear waste forms for high-level radioactive waste, Prog. Nucl. Energ. **29**, 63 (1995).

[3] M. Ferhi, K. Horchani-Naifer, and M. Férid, Combustion synthesis and luminescence properties of LaPO₄: Eu (5%), J. Lumin. **128**, 1777 (2008).

[4] E. Chaudan, J. Kim, S. Tusseau-Nenez, P. Goldner, O. L. Malta, J. Peretti, and T. Gacoin, Polarized luminescence of anisotropic LaPO₄ : Eu nanocrystal polymorphs, J. Am. Chem. Soc. **140**, 9512 (2018).

[5] R. S. de Oliveira, B. S. de Brito, J. Kulesza, S. Alves-Jr, and B. S. Barros, Tunable photoluminescence of nanostructured $LaPO_4:Eu^{3+}/Tb^{3+}$ synthesized via a microwave-assisted ethylene glycol route, Ceram. Inter. **43**, 8276 (2017).

[6] R. C. Ewing and L. M. Wang, Phosphates as nuclear waste forms, Rev. Min. Geochem. **48**, 673 (2002).

[7] W. J. Weber, A. Navrotsky, S. Stefanovsky, E. Vance, and E. Vernaz, Materials science of high-level nuclear waste immobilization, MRS Bull. **34**, 46 (2009).

[8] R. D. Shannon, Revised effective ionic radii and systematic studies of interatomic distances in halides and chaleogenides, Acta Crystallogr. **A32**, 751 (1976).

[9] P. M. Kowalski, G. Beridze, V. L. Vinograd, and D. Bosbach, Heat capacities of lanthanide and actinide monazite-type ceramics, J. Nuc. Mater. **464**, 147 (2015).

[10] A. Thust, Y. Arinicheva, E. Haussühl, J. Ruiz-Fuertes, L. Bayarjargal, S. C. Vogel, S. Neumeier, and B. Winkler, Physical properties of $La_{1-x}Eu_xPO_4$, $0 \leqslant x \leqslant 1$, monazite type ceramics, J. Am. Ceram. Soc. **98**, 4016 (2015).

[11] X. Wang, Y. Teng, Y. Huang, L. Wu, and P. Zeng, Synthesis and structure of $Ce_{1-x}Eu_xPO_4$ solid solutions for minor actinides immobilization, J. Nuclear. Mater. **451**, 147 (2014).

[12] P. M. Kowalski, Y. Ji, Y. Li, Y. Arinicheva, G. Beridze, S. Neumeier, A. Bukaemskiy, and D. Bosbach, Simulation of ceramic materials relevant for nuclear waste management: Case of $La_{1-x}Eu_xPO_4$ solid solution, Nucl. Instr. Meth. Phys. Res. B **393**, 68 (2017).

[13] T. Geisler, K. Popa, and R. J. M. Konings, Evidence for lattice strain and non-ideal behavior in the $(La_{1-x}Eu_x)PO_4$ solid solution from X-ray diffraction and vibrational spectroscopy, Front. Earth Sci. **4**, 64 (2016).

[14] A. C. Palke and J. F. Stebbins, Paramagnetic interactions in the ³¹P NMR spectroscopy of rare earth element orthophosphate ($REPO_4$, monazite/xenotime) solid solutions, Am. Miner. **96**, 1343 (2011).

[15] A. C. Palke, J. F. Stebbins, and L. A. Boatner, ³¹P magic angle spinning NMR study of flux-grown rare-earth element orthophosphate (monazite/xenotime) solid solutions: Evidence of random cation distribution from paramagnetically shifted NMR resonances, Inorg. Chem. **52**, 12605 (2013).

[16] X. Deschanels, V. Picot, B. Glorieux, F. Jorion, S. Peuget, D. Roudil, C. Jegou, V. Broudic, J.N. Cachia, T. Advocat, C. Den Auwer, C. Fillet, J. P. Coutures, C. Hennig, and A. Scheinost, Plutonium incorporation in phosphate and titanate ceramics for minor actinide containment, J. Nucl. Mater. **352**, 233 (2006).

[17] D. Bregiroux, R. Belin, P. Valenza, F. Audubert, and D. Bernache-Assollant, Plutonium and americium monazite materials: solid state synthesis and X-ray diffraction study, J. Nucl. Mater. **366**, 52 (2007).

[18] Y. Arinicheva, K. Popa, A. C. Scheinost, A. Rossberg, O. Dieste-Blanco, P. Raison, A. Cambriani, J. Somers, D. Bosbach, and S. Neumeier, Structural investigations of (La, Pu)PO₄ monazite solid solutions: XRD and XAFS study, J. Nuc. Mater. **493**, 404 (2017).

[19] D. Bregiroux, F. Audubert, T. Charpentier, D. Sakellariou, and D. Bernache-Assollant, Solid-state synthesis of monazite-type compounds LnPO₄ (Ln = La to Gd), Solid State Sci. **9**, 432 (2007).

[20] M. Bose, M. Bhattacharya, and S. Gangue, ³¹P NMR studies of transferred hyperfme effects in rare-earth orthophosphates, Phys. Rev. B **19**, 72 (1979).

[21] S. Maron, G. Dantelle, T. Gacoin, and F. Devreux, NMR and ESR relaxation in Nd- and Gd- doped LaPO₄: Towards the accurate determination of doping concentration, Phys. Chem. Chem. Phys. **16**, 18788 (2014).

[22] S. Maron, N. Ollier, T. Gacoin, and G. Dantelle, Determination of paramagnetic concentrations inside a diamagnetic matrix using solid-state NMR, Phys. Chem. Chem. Phys. **19**, 12175 (2017).

[23] H. M. McConnell and R. E. Robertson, Isotropic nuclear resonance shifts, J. Chem. Phys. **29**, 1361 (1958).

[24] A. J. Pell, G. Pintacunda, and C. P. Grey, Paramagnetic NMR in solution and the solid state, Prog. Nucl. Magn. Reson. Spect. **111**, 1 (2019).

[25] T. O. Pennanen and J. Vaara, Nuclear Magnetic Resonance Chemical Shift in an Arbitrary Electronic Spin State, Phys. Rev. Lett. **100**, 133002 (2008).

[26] B. Bleaney, Nuclear magnetic resonance shifts in solution due to lanthanide ions, J. Magn. Reson. (1969) **8**, 91 (1972).

[27] I. Bertini, C. Luchinat, and G. Parigi, Magnetic susceptibility in paramagnetic NMR, Prog. Nuc. Magn. Reson. Spect. **40**, 249 (2002).

[28] H. M. Mcconnell, Theory of nuclear magnetic shielding in molecules. I. Long range dipolar shielding of protons, J. Chem. Phys. **27**, 226 (1957).

[29] R. M. Golding and P. Pyykkö, On the theory of pseudocontact NMR shifts due to lanthanide complexes, Mol. Phys. **26**, 1389 (1973).

[30] R. M. Golding and M. P. Halton, A theoretical study of ^{14}N and ^{17}O NMR shifts in lanthanide complexes, Aust. J. Chem. **25**, 2577 (1972).

[31] S. Moon and S. Patchkovskii, *First-Principles Calculations of Paramagnetic NMR Shifts. Calculation of NMR and EPR Parameters. Theory and Applications*, edited by M. Kaupp, M. Bühl, and V. G. Malkin (Wiley- VCH, Weinheim, 2004), pp. 325–338.

[32] R. Martin and J. Autschbach, Temperature dependence of contact and dipolar NMR chemical shifts in paramagnetic molecules, J. Chem. Phys. **142**, 054108 (2015).

[33] A. Soncini and W. Van den Heuvel, Paramagnetic NMR chemical shift in a spin state subject to zero-field splitting, J. Chem. Phys. **138**, 021103 (2013).

[34] J. Autschbach, S. Patchkovskii, and B. Pritchard, Calculation of hyperfine tensors and paramagnetic NMR shifts using the relativistic zeroth-order regular approximation and density functional theory, J. Chem. Theory Comput. **7**, 2175 (2011).

[35] L. Banci, I. Bertini, G. G. Savellini, A. Romagnoli, P. Turano, M. A. Cremonini, C. Luchinat, and H. B. Gray, Pseudocontact shifts as constraints for energy minimization and molecular dynamics calculations on solution structures of paramagnetic metalloproteins, Proteins **29**, 68 (1997).

[36] E. A. Suturina and I. Kuprov, Pseudocontact shifts from mobile spin labels, Phys. Chem. Chem. Phys. **18**, 26412 (2016).

[37] G. Castro, M. Regueiro-Figuero, D. Esteban-Gómez, R. Bastida, A. Macías, P. Pérez-Lourido, C. Platas-Iglesias, and L. Valencia, Exceptionally inert lanthanide(III) PARACEST MRI contrast agents based on an 18-membered macrocyclic platform, Chem. Eur. J. **21**, 18662 (2015).

[38] G. Castro, M. Regueiro-Figueroa, D. Esteban-Gómez, P. Pérez-Lourido, C. Platas-Iglesias, and L. Valencia, Magnetic anisotropies in rhombic lanthanide(III) complexes do not conform to Bleaney's theory, Inorg. Chem. **55**, 3490 (2016).

[39] C. Dee, D. Esteban-Gómez, C. Platas-Iglesias, and M. Seitz, Long wavelength excitation of Europium luminescence in extended, carboline-based cryptates, Inorg. Chem. **57**, 7390 (2018).

[40] A. M. Kenwright, I. Kuprov, E. De Luca, D. Parker, S. U. Pandya, P. K. Senanayake, and D. G. Smith, ^{19}F NMR based pH probes: Lanthanide(III) complexes with pH-sensitive chemical shifts, Chem. Commun. **0**, 2514 (2008).

[41] P. Harvey, K. H. Chalmers, E. De Luca, A. Mishra, and D. Parker, Paramagnetic ^{19}F chemical shift probes that respond selectively to calcium or citrate levels and signal ester hydrolysis, Chem. Eur. J. **18**, 8748 (2012).

[42] A. M. Funk, K. N. A. Finney, P. Harvey, A. M. Kenwright, E. R. Neil, N. J. Rogers, P. Kanthi Senanayake, and D. Parker, Critical analysis of the limitations of Bleaney's theory of magnetic anisotropy in paramagnetic lanthanide coordination complexes, Chem. Sci. **6**, 1655 (2015).

[43] E. A. Suturina, K. Mason, C. F. G. C. Geraldes, I. Kuprov, and D. Parker, Beyond Bleaney's theory: Experimental and theoretical analysis of periodic trends in lanthanide-induced chemical shift, Angew. Chem. Int. Ed. **56**, 12215 (2017).

[44] M. Vonci, K. Mason, E. A. Suturina, A. T. Frawley, S. G. Worswick, I. Kuprov, D. Parker, E. J. L. McInnes, and N. F. Chilton, Rationalization of anomalous pseudocontact shifts and their solvent dependence in a series of C_3-symmetric lanthanide complexes, J. Am. Chem. Soc. **139**, 14166 (2017).

[45] L. Banci, I. Bertini, L. K. Bren, A. M. Cremonini, B. H. Gray, C. Luchinat, and P. Turano, The use of pseudocontact shifts to refine solution structures of paramagnetic metalloproteins: Met80Ala cyano-cytochrome c as an example, JBIC, J. Biol. Inorg. Chem. **1**, 117 (1996).

[46] I. Bertini, C. Luchinat, and G. Parigi (Eds.), *NMR of Biomolecules: Towards Mechanistic Systems Biology* (Wiley-Blackwell, 2012), p. 154.

[47] M. A. S. Hass and M. Ubbink, Structure determination of protein-protein complexes with long-range anisotropic paramagnetic NMR restraints, Curr. Opin. Struct. Biol. **24**, 45 (2014).

[48] I. Bertini, M. B. L. Janik, Y.-M. Lee, C. Luchinat, and A. Rosato, Magnetic susceptibility tensor anisotropies for a lanthanide ion series in a fixed protein matrix, J. Am. Chem. Soc. **123**, 4181 (2001).

[49] N. C. George, A. J. Pell, G. Dantelle, K. Page, A. Llobet, M. Balasubramanian, G. Pintacuda, B. F. Chmelka, and R. Seshadri, Local Environments of Dilute Activator Ions in the Solid-State Lighting Phosphor Y$_{3-x}$Ce$_x$Al$_5$O$_{12}$, Chem. Mater. **25**, 3979 (2013).

[50] C. P Grey, M. E. Smith, A. K. Cheetham, C. M. Dobson, and R. Dupree, Yttrium-89 magic angle spinning NMR study of rare-earth pyrochlores: Paramagnetic shifts in the solid state, J. Am. Chem. Soc. **112**, 4670 (1990).

[51] A. K. Cheetham, C. M. Dobson, C. P. Grey, and R. J. B. Jakeman, Paramagnetic shift probes in high-resolution solid-state NMR, Nature **328**, 706 (1987).

[52] C. P. Grey, C. M. Dobson, A. K. Cheetham, and R. J. B. Jakeman, Studies of rare-earth stannates by trin-119 MAS NMR. The use of paramagnetic shift probes in the solid state, J. Am. Chem. Soc. **111**, 505 (1989).

[53] K. R. Thurber and R. Tycko, Measurement of sample temperatures under magic-angle spinning from the chemical shift and spin-lattice relaxation rate of ^{79}Br in KBr powder, J. Magn. Reson. **196**, 84 (2009).

[54] D. Massiot, F. Fayon, M. Capron, I. King, S. Le Calvé, B. Alonso, J.-O. Durand, B. Bujoli, Z. Gan, and G. Hoatson, Modelling one- and two-dimensional solid-state NMR spectra, Magn. Reson. Chem. **40**, 70 (2002).

[55] J. J. Baldoví, S. Cardona-Serra, J. M. Clemente-Juan, E. Coronado, A. Gaita-Arino, and A. Palii, SIMPRE: A

software package to calculate crystal field parameters, energy levels, and magnetic properties on mononuclear lanthanoid complexes based on charge distributions, J. Comput. Chem. **34**, 1961 (2013).

[56] J. J. Baldoví, J. J. Borrás-Almenar, J. M. Clemente-Juan, E. Coronado, and A. Gaita-Ariño, Modeling the properties of lanthanoid single-ion magnets using an effective point-charge approach, Dalton Trans. **41**, 13705 (2012).

[57] M. Speldrich, H. Schilder, H. Lueken, and P. Kögerler, A computational framework for magnetic polyoxometalates and molecular spin structures: CONDON 2.0, Isr. J. Chem. **51**, 215 (2011).

[58] P. Giannozzi, S. Baroni, N. Bonini, M. Calandra, R. Car, C. Cavazzoni, D. Ceresoli, G. L. Chiarotti, M. Cococcioni, I. Dabo, A. Dal Corso, S. de Gironcoli, S. Fabris, G. Fratesi, and R. Gebauer *et al.*, QUANTUM ESPRESSO: A modular and open-source software project for quantum simulations of materials, J. Phys.: Condens. Matter. **21**, 395502 (2009).

[59] T. Charpentier, S. Ispas, M. Profeta, F. Mauri, and C. J. Pickard, First-principles calculation of ^{17}O, ^{29}Si, and ^{23}Na NMR spectra of sodium silicate crystals and glasses, J. Phys. Chem. B **108**, 4147 (2004).

[60] T. Charpentier, The PAW/GIPAW approach for computing NMR parameters: a new dimension added to NMR study of solids, Solid State NMR **40**, 1 (2011).

[61] See Supplemental Material at http://link.aps.org/supplemental/10.1103/PhysRevB.100.054412 for additional crystallographic, NMR, magnetic susceptibility and XPS experimental data for the whole $La_xEu_{1-x}PO_4$ series; full theoretical energy levels and CFP data; and description of the small clusters used for DFT calculations.

[62] M. J. Frisch *et al.*, GAUSSIAN 09, Revision D.01. (Gaussian, Inc., Wallingford CT, 2010).

[63] J. Autschbach and B. Pritchard, Calculation of molecular g-tensors using the zeroth-order regular approximation and density functional theory: Expectation value versus linear response approaches, Theor. Chem. Acc. **129**, 453 (2011).

[64] P. Hrobárik, R. Reviakine, A. V. Arbuznikov, O. L. Malkina, V. G. Malkin, F. H. Köhler, and M. Kaupp, Density functional calculations of NMR shielding tensors for paramagnetic systems with arbitrary spin multiplicity: Validation on 3d metallocenes, J. Chem. Phys. **126**, 024107 (2007).

[65] Amsterdam Density Functional (ADF), SCM Theoretical Chemistry, Vrije Universiteit: Amsterdam, The Netherlands, 2017, http://www.scm.com.

[66] G. te Velde, F. M. Bickelhaupt, E. J. Baerends, C. Fonseca Guerra, S. J. A. van Gisbergen, J. G. Snijders, and T. Ziegler, Chemistry with ADF, J. Comput. Chem. **22**, 931 (2001).

[67] E. van Lenthe, E. J. Baerends, and J. G. Snijders, Relativistic total energy using regular approximations, J. Chem. Phys. **101**, 9783 (1994).

[68] O. V. Gritsenko, P. R. T. Schipper, and E. J. Baerends, Approximation of the exchange-correlation Kohn–Sham potential with a statistical average of different orbital model potentials, Chem. Phys. Letters **302**, 199 (1999).

[69] P. R. T. Schipper, O. V. Gritsenko, S. J. A. van Gisbergen, and E. J. Baerends, Molecular calculations of excitation energies and (hyper)polarizabilities with a statistical average of orbital model exchange-correlation potentials, J. Chem. Phys. **112**, 1344 (2000).

[70] E. van Lenthe and E. J. Baerends, Optimized Slater-type basis sets for the elements 1–118, J. Comput. Chem. **24**, 1142 (2003).

[71] J. Autschbach, Magnitude of finite-nucleus-size effects in relativistic density functional computations of indirect NMR Nuclear spin–spin coupling constants, Chem. Phys. Chem. **10**, 2274 (2009).

[72] Wolfram Research, Inc., MATHEMATICA, Version 10, Wolfram Research, Inc., Champaign, Illinois, 2018.

[73] D. F. Mullica, D. A. Grossie, and L. A. Boatner, Coordination geometry and structural determinations of $SmPO_4$, $EuPO_4$ and $GdPO_4$, Inorg. Chim. Acta **109**, 105 (1985).

[74] G. W. Beal, L. A. Boatner, D. F. Mullica, and W. O. Milligan, The structure of cerium orthophosphate, a synthetic analogue of monazite, J. Inorg. Nucl. Chem. **43**, 101 (1981).

[75] F. C. Strobridge, D. S. Middlemiss, A. J. Pell, M. Leskes, R. J. Clement, F. Pourpoint, Z. Lu, J. V. Hanna, G. Pintacuda, L. Emsley, A. Samoson, and C. P. Grey, Characterising local environments in high energy density Li-ion battery cathodes: A combined NMR and first principles study of $LiFe_xCo_{1-x}PO_4$, J. Mater. Chem. A **2**, 11948 (2014).

[76] A. Bronova, N. Kannengießer, and R. Glaum, Optical spectra and magnetic behavior of a wide range of europium(III) oxo-compounds: Analysis of the ligand-field effects, Inorg. Chem. **56**, 9235 (2017).

[77] S. Golbs, F. M. Schappacher, R. Pöttgen, R. Cardoso-Gil, A. Ormeci, U. Schwarz, W. Schnelle, Y. Grin, and M. Schmidt, Europium phosphate, europium arsenate, and europium antimonate - correlation of crystal structure and physical properties, Z. Anorg. Allg. Chem. **639**, 2139 (2013).

[78] Y. Takikawa, S. Ebisu, and S. Nagata, Van Vleck paramagnetism of the trivalent Eu ions, J. Phys. Chem. Solids **71**, 1592 (2010).

[79] P. Caro and P. Porcher, The paramagnetic susceptibility of c-type europium sesquioxide, J. Magn. Magn. Mater. **58**, 61 (1986).

[80] N. L. Huang and J. H. Van Vleck, Effect of the anisotropic exchange and the crystalline field on the magnetic susceptibility of Eu_2O_3, J. Appl. Phys. **40**, 1144 (1969).

[81] J. H. Van Vleck, On dielectric constants and magnetic susceptibilities in the new quantum mechanics Part III—application to dia- and paramagnetism, Phys. Rev. **31**, 587 (1928).

[82] A. Frank, Temperature variation of the magnetic susceptibility, gyromagnetic ratio, and heat capacity in Sm^{3+} and Eu^{3+}, Phys. Rev. **39**, 119 (1932).

[83] K. Popa, M. Cologna, L. Martel, D. Staicu, A. Cambriani, M. Ernstberger, P. E. Raison, and J. Somers, $CaTh(PO_4)_2$ cheralite as a candidate ceramic nuclear waste form: Spark plasma sintering and physicochemical characterisation, J. Eur. Ceram. Soc. **36**, 4115 (2016).

[84] I. J. Lowe and D. Tse, Nuclear spin-lattice relaxation via paramagnetic centers, Phys. Rev. **166**, 279 (1968).

[85] E. Terazzi, J.-P. Rivera, N. Ouali, and C. Piguet, A justification for using NMR model-free methods when investigating the solution structures of rhombic paramagnetic lanthanide complexes, Magn. Reson. Chem. **44**, 539 (2006).

[86] B. Bleaney, M. Dobson, A. Levine, B. Martin, J. P. Williams, and A. V. Xavier, Origin of lanthanide nuclear magnetic resonance shifts and their uses, J. Chem. Soc. Chem. Comm. **0**, 791b (1972).

[87] J. A. Peters, J. Huskens, and D. J. Raber, Lanthanide induced shifts and relaxation rate enhancements, Prog. Nucl. Magn. Reson. Spectrosc. **28**, 283 (1996).

[88] W. B. Lewis, S. W. Rabideau, N. H. Krikorian, and W. G. Witteman, Knight shifts of ^{13}C in the carbides of uranium and thorium, Phys. Rev. **170**, 455 (1968).

[89] W. B. Lewis, J. A. Jackson, J. F. Lemons, and H. Taube, Oxygen17 NMR shifts in aqueous solutions of rare earth ions, J. Chem. Phys. **36**, 694 (1962).

[90] E. Colineau, J. P. Sanchez, J. Rebizant, and J. M. Winand, Hyperfine interaction parameters in GdPd$_2$Al$_3$ and ground state of CePd$_2$Al$_3$ and NpPd$_2$Al$_3$, Solid State Comm. **92**, 915 (1994).

[91] S. Edvardsson and M. Klinterberg, Role of the electrostatic model in calculating rare-earth crystal-field parameters, J. Alloys Compd. **275–277**, 230 (1998).

[92] C.V. Tomy, R. Nagarajan, S.K. Malik, R. Prasad, N. C. Soni, and K. Adhikary, Magnetic susceptibility, resistivity and ^{151}Eu Mössbauer studies on Zn-substituted EuBa$_2$Cu$_3$O$_{7-y}$, Solid State Comm. **75**, 59 (1990).

[93] B. Anke, S. Hund, C. Lorent, O. Janka, T. Block, R. Pöttgen, and M. Lerch, Synthesis, crystal structure, and magnetic properties of pyrochlore-type Eu$_2$Ta$_2$(O, N)$_{7+\delta}$, Z. Anorg. Allg. Chem. **643**, 1824 (2017).

[94] D. Petrov, B. Angelov, and V. Lovchinov, Magnetic susceptibility and surface properties of EuAlO$_3$ nanocrystals, J. Alloys Comp. **509**, 5038 (2011).

[95] C. Cascales, R. Sáez-Puche, and P. Porcher, Crystal-field effect on the magnetic susceptibility of rare-earth (Pr, Nd, Eu) mixed oxides, J. Solid State Chem. **114**, 52 (1995).

[96] V. Spasojević, M. Dramićanin, V. Jokanović, Ž. Andrić, J. Blanuša, V. Kusigerski, M. Mitrić, M. Tadić, and A. Kapičić, Magnetic properties of nanostructured SiO$_2$: Eu^{3+} powders, J. Serb. Chem. Soc. **71**, 413 (2006).

[97] D. Akahoshi, S. Koshikawa, T. Nagase, E. Wada K. Nishina, R. Kajihara, H. Kuwahara, and T. Saito, Magnetic phase diagram for the mixed-valence Eu oxide EuTi$_{1-x}$Al$_x$O$_3$ (0 ⩽ x ⩽ 1), Phys. Rev. B **96**, 184419 (2017).

[98] M. Radzi-eowski, F. Stegemann, T. Block, J. Stahl, D. Johrendt, and O. Janka, Abrupt europium valence change in Eu$_2$Pt$_6$Al$_{15}$ around 45 K, J. Am. Chem. Soc. **140**, 8950 (2018).

[99] C. L. Chien and A. W. Sleight, Mössbauer effect studies of euroiuum pyrochlores, Phys. Rev. B **18**, 2031 (1978).

[100] A. Błachowski, K. Ruebenbauer, J. Zukrowski, Z. Bukowski, K. Rogacki, P. J. W. Moll, and J. Karpinski, Interplay between magnetism and superconductivity in EuFe$_{2-x}$Co$_x$As$_2$ studied by ^{57}Fe and ^{151}Eu Mössbauer spectroscopy, Phys. Rev. B **84**, 174503 (2011).

[101] H. Akamatsu, K. Fujita, S. Murai, and K. Tanaka, Ferromagnetic Eu^{2+}-based oxide glasses with reentrant spin glass behavior, Phys. Rev. B **81**, 014423 (2010).

[102] L. A. Zavala-Sanchez, G. A. Hirata, E. Novitskaya, K. Karandikar, M. Herrera, and O. A. Graeve, Distribution of Eu^{2+} and Eu^{3+} ions in hydroxyapatite: A cathodoluminescence and Raman study, ACS Biomater. Sci. Eng. **1**, 1306 (2015).

[103] T. Maruyama, S. Morishima, H. Bang, K. Akimoto, and Y. Nanishi, Valence transition of Eu ions in GaN near the surface, J.Crystal Growth **237–239**, 1167 (2002).

[104] R. Vercaemst, D. Poelman, L. Fiermans, R. L. Van Meirhaeghe, W. H. Laflère, and F. Cardon, A detailed XPS study of the rare earth compounds EuS and EuF$_3$, J. Electron Spectrosc. Relat. Phenom. **74**, 45 (1995).

[105] A. Frank, The effect of crystalline fields on the magnetic susceptibilities of Sm^{3+} and Eu^{3+}, and the heat capacity of Sm^{3+}, Phys. Rev. **48**, 765 (1935).

[106] K. Binnemans, Interpretation of europium(III) spectra, Coordination Chemistry Reviews **295**, 1 (2015).

[107] E. Antic-Fidancev, J. Hölsa, M. Lemaitre-Blaise, and P. Porcheri, Simulation of the energy level scheme of Nd^{3+} and Eu^{3+} ions in rare-earth orthovanadates and phosphates, J. Phys. Condens. Matter. **3**, 6829 (1991).

[108] D. Neogy, P. K. Chakrabarti, K. N. Chattopadhyay, and B. M. Wanklyn, Experimental and theoretical studies on the magnetic behaviour of Nd^{3+} in NdPO$_4$, J. Magn. Magn. Mater. **173**, 167 (1997).

[109] E. Rukmini, C. K. Jayasankar, and M. F. Reid, Correlation-crystal-field analysis of Nd^{3+}(4f^3) energy-level structures in various crystal hosts, J. Phys. Condens. Mater. **6**, 5919 (1994).

[110] G. Chen, J. Hölsa, and J. R. Peterson, Luminescence study of single-crystal EuPO$_4$ at high pressure, J. Phys. Chem. Solids **58**, 2031 (1997).

[111] M. Rappaz, M. M. Abraham, J. O. Ramey, and L. A. Boatner, EPR spectroscopic characterization of Gd^{3+} in the monazite-type rare-earth orthophosphates: LaPO$_4$, CePO$_4$, PrPO$_4$, NdPO$_4$, SmPO$_4$, and EuPO$_4$, Phys. Rev. B **23**, 1012 (1981).

[112] A. Mondal, M. W. Gaultois, A. J. Pell, M. Iannuzzi, C. P. Grey, J. Hutter, and M. Kaupp, Large-scale computation of NMR shifts for paramagnetic solids using CP2K, J. Chem. Theory Comput. **14**, 377 (2018).

[113] A. Mondal and M. Kaupp, Computation of NMR shifts for paramagnetic solids including zero-field-splitting and beyond-DFT approaches. Application to LiMPO$_4$ (M = Mn, Fe, Co, Ni) and MPO$_4$ (M = Fe, Co), J. Phys. Chem. C **123**, 8387 (2019).

[114] J. Novotný, M. Sojka, S. Komorovsky, M. Nečas, and R. Marek, Interpreting the paramagnetic NMR spectra of potential Ru(III) metallodrugs: Synergy between experiment and relativistic DFT calculations, J. Am. Chem. Soc. **138**, 8432 (2016).

[115] A. A. Pinkerton, M. Rower, and S. Spiliadis, Lanthanide-induced contact shifts. The average electron spin polarization, theory and experiment, J. Magn. Reson. (1969) **64**, 420 (1985).